nature cell biology

Chronic p53-independent p21 expression causes genomic instability by deregulating replication licensing

Panagiotis Galanos[1,17], Konstantinos Vougas[2,17], David Walter[3], Alexander Polyzos[2], Apolinar Maya-Mendoza[4], Emma J. Haagensen[5], Antonis Kokkalis[2], Fani-Marlen Roumelioti[2], Sarantis Gagos[2], Maria Tzetis[6], Begoña Canovas[7], Ana Igea[7], Akshay K. Ahuja[8], Ralph Zellweger[8], Sofia Havaki[1], Emanuel Kanavakis[6,9], Dimitris Kletsas[10], Igor B. Roninson[11], Spiros D. Garbis[12], Massimo Lopes[8], Angel Nebreda[7,13], Dimitris Thanos[2], J. Julian Blow[5], Paul Townsend[14], Claus Storgaard Sørensen[3], Jiri Bartek[4,15,16,18] and Vassilis G. Gorgoulis[1,2,14,18]

The cyclin-dependent kinase inhibitor p21[WAF1/CIP1] (p21) is a cell-cycle checkpoint effector and inducer of senescence, regulated by p53. Yet, evidence suggests that p21 could also be oncogenic, through a mechanism that has so far remained obscure. We report that a subset of atypical cancerous cells strongly expressing p21 showed proliferation features. This occurred predominantly in p53-mutant human cancers, suggesting p53-independent upregulation of p21 selectively in more aggressive tumour cells. Multifaceted phenotypic and genomic analyses of p21-inducible, p53-null, cancerous and near-normal cellular models showed that after an initial senescence-like phase, a subpopulation of p21-expressing proliferating cells emerged, featuring increased genomic instability, aggressiveness and chemoresistance. Mechanistically, sustained p21 accumulation inhibited mainly the CRL4–CDT2 ubiquitin ligase, leading to deregulated origin licensing and replication stress. Collectively, our data reveal the tumour-promoting ability of p21 through deregulation of DNA replication licensing machinery—an unorthodox role to be considered in cancer treatment, since p21 responds to various stimuli including some chemotherapy drugs.

Numerous proteins involved in key cellular processes display bimodality in cancer, acting as either tumour suppressors or oncoproteins (Supplementary Table 1). This phenomenon is commonly attributed to 'cellular or environmental context'. Elucidating the mechanism(s) underlying such context-dependent duality is essential for rational design of cancer therapy.

The cyclin-dependent kinase inhibitor (CDKI) p21 (p21) is a pivotal downstream effector of the tumour-suppressor p53, mediating mainly G1-phase arrest and cellular senescence in response to various stimuli[1]. Several studies suggest that p21 can also manifest oncogenic properties (Supplementary Table 1). In some studies, the oncogenic function of p21 was credited to unconventional cytoplasmic localization of p21 that inactivates pro-apoptotic proteins[2,3]. Still, in most cases the underlying mechanism remains obscure. Notably, while p53 is frequently mutated in cancer[4], *p21* is rarely affected genetically[1,5]. The latter would be logical if p21 operated exclusively within the p53 pathway. However, p21 is activated also by diverse p53-independent signals[1].

[1]Molecular Carcinogenesis Group, Department of Histology and Embryology, School of Medicine, University of Athens, 75 Mikras Asias Str, Athens GR-11527, Greece. [2]Biomedical Research Foundation of the Academy of Athens, 4 Soranou Ephessiou St., Athens GR-11527, Greece. [3]Biotech Research and Innovation Centre (BRIC), University of Copenhagen, Ole Maaloes Vej 5, Copenhagen DK-2200, Denmark. [4]Genome Integrity Unit, Danish Cancer Society Research Centre, Strandboulevarden 49, Copenhagen DK-2100, Denmark. [5]Centre for Gene Regulation & Expression, College of Life Sciences, University of Dundee, Dow Street, Dundee DD1 5EH, UK. [6]Department of Medical Genetics, Medical School, University of Athens, Thivon & Levadias Str., Athens GR-11527, Greece. [7]Institute for Research in Biomedicine (IRB Barcelona), Barcelona Institute of Science and Technology, 08028 Barcelona, Spain. [8]Institute of Molecular Cancer Research, University of Zurich, Winterthurerstrasse 190, Zurich CH-8057, Switzerland. [9]Research Institute for the Study of Genetic and Malignant Disorders in Childhood, Aghia Sophia Children's Hospital, Thivon Str., Athens GR-11527, Greece. [10]Laboratory of Cell Proliferation and Ageing, Institute of Biosciences and Applications, National Centre for Scientific Research 'Demokritos', Agia Paraskevi Attikis, PO Box 60228, Athens GR-153 10, Greece. [11]Center for Targeted Therapeutics, Department of Drug Discovery and Biomedical Sciences, South Carolina College of Pharmacy, University of South Carolina, Coker Life Science Building, 715 Sumter Street, Columbia, South Carolina 29208, USA. [12]Cancer and Clinical Experimental Science Units, Faculty of Medicine, Institute for Life Sciences, Center for Proteome Research, University of Southampton, University Road Southampton, Southampton SO17 1BJ, UK. [13]Institució Catalana de Recerca i Estudis Avançats (ICREA), 08010 Barcelona, Spain. [14]Faculty Institute of Cancer Sciences, University of Manchester, Manchester Academic Health Science Centre, Wilmslow Road, Manchester M20 4QL, UK. [15]Institute of Molecular and Translational Medicine, Faculty of Medicine and Dentistry, Palacky University, Hněvotínská, Olomouc 1333/5 779 00, Czech Republic. [16]Science for Life Laboratory, Division of Translational Medicine and Chemical Biology, Department of Medical Biochemistry and Biophysics, Karolinska Institute, Stockholm SE-171 77, Sweden. [17]These authors contributed equally to this work. [18]Correspondence should be addressed to J.B. or V.G.G. (e-mail: jb@cancer.dk or vgorg@med.uoa.gr)

Replication licensing ensures that genome replication takes place once per cell cycle[6,7], due to the periodic expression of the replication licensing factors (RLFs) ORC, CDT1 and CDC6 that increase in late M to G1 phases and decrease in S/G2 phases[8]. Deregulation of the replication licensing process promotes genomic instability and tumorigenicity, mainly via unscheduled DNA re-replication[9–12]. Aberrant expression of RLFs occurs in diverse malignancies[13,14]. Here we present a pathophysiological mechanism demonstrating that protracted p21 expression, in a p53 loss-of-function environment, causes deregulation of the replication licensing machinery, replication stress and genomic instability.

RESULTS

A subset of atypical p21-expressing cells in advanced-stage tumours and preneoplastic lesions show signs of proliferation

In an array of human tumours we observed an intriguing relationship between p21 and the proliferation marker Ki67. While the anticipated mutually exclusive expression pattern of p21 and Ki67 was prevalent, consistent with the growth-inhibitory properties of p21, there were a number of atypical cancer cells co-expressing p21 and Ki67 (Fig. 1a–c). Atypical cancer cells commonly point to adverse prognosis[15]. Most of the carcinomas examined displayed p53 alterations[13,14,16]. In preneoplastic lesions with p53 aberrations we noticed a similar phenomenon (Fig. 1d)[17]. The unexpected co-expression of p21 with Ki67 suggests either tolerance to high p21 levels, or selection under chronic p21 expression allowing for emergence of a subpopulation of p21-positive cells that regained proliferative capacity and possibly acquired enhanced aggressiveness.

p53-independent expression of p21 upregulates RLFs

To address the impact of constitutive p21 expression in a p53-deficient context we employed two doxycycline-inducible (Tet-ON) p21-expressing cellular systems: one recapitulating the cancerous stage, based on Saos2, a p53-null human osteosarcoma cell line (Saos2 p21 Tet-ON), and the other reflecting the precancerous stage by expressing the inducible module in the Li–Fraumeni-derived fibroblasts (MDAH041-Li–Fraumeni p21 Tet-ON) (Fig. 1e). The MDAH041 fibroblasts are p53-null human cells, considered 'near'-normal, as they are reminiscent of normal diploid cells when p53 is restored, suggesting that their downstream functions are largely intact[18].

To avoid heterogeneity of p21 expression in bulk cell cultures, we isolated p21-inducible clones that expressed p21 levels comparable to those observed *in vivo* and in cells exposed to genotoxic agents or p53-independent p21-inducing stimuli (such as TGF-β)[1] (Fig. 1e). Apart from monitoring cell proliferation, transcriptome and proteome landscapes were examined at distinct time points (Fig. 1e) after p21 induction to identify candidate pathways/networks that could over time exercise an 'oncogenic' effect (Supplementary Tables 2–9). Representative high-throughput results were confirmed independently by quantitative real-time PCR and immunoblotting (Fig. 2a and Supplementary Fig. 1ai–ii). As expected[19], the p21-expressing clones reduced their growth rate and progressively acquired a senescent phenotype that peaked around day 10 (Supplementary Fig. 1b and Supplementary Videos 1–3). Consistent with such phenotypical changes, Gene Ontology biological process enrichment analyses revealed suppression of key 'mitosis' factors

(Supplementary Fig. 1a and Supplementary Tables 2–9). Unexpectedly and counter-intuitively, the proteome analysis revealed prominent upregulation of the RLFs: CDT1, CDC6 and ORC ($P = 1.5 \times 10^{-6}$); with CDT1 protein increase being the earliest biochemical alteration among all measured parameters (Supplementary Tables 2–9). The increase of the RLFs was not accompanied by elevated messenger RNA, implying post-transcriptional regulation (Fig. 2a). Similar results were observed in the Li–Fraumeni p21-inducible cells (Fig. 2b). Notably, p21, CDT1 and CDC6 share the same E3-ubiquitin ligase, CRL4–CDT2 (refs 8,20). Continuous p21 expression might saturate its enzymatic activity leading to CDT1 and CDC6 accumulation (Fig. 2c). Consistently, SET8 methyltransferase, a known target of CRL4–CDT2 (ref. 21), was upregulated after p21 induction (Fig. 2c). Shutting-off p21, after a period of induction, led to a ubiquitylation-dependent decrease of CDT1 (Fig. 2d). Furthermore, transiently expressed mutant p21$^{(mut)PCNA}$, which avoids p21 degradation by CRL4–CDT2, did not augment CDT1 and CDC6 abundance (Fig. 2e)[20]. Also, induction of wild-type p21, but not the p21$^{(mut)PCNA}$ mutant, resulted in CDT1 and CDC6 accumulation (Fig. 2f). Given that p21 has the strongest affinity amongst all PCNA-interacting proteins ($K_d \sim 2.5$ nM) (ref. 22) these results strongly support a mechanism whereby excessive p21 saturates its own ubiquitin ligases allowing accumulation of other targets such as CDT1 and CDC6. The increase of G1-phase cells caused by p21 induction possibly also contributed to the observed reduced RLF protein turnover, as RLFs are normally protected from degradation in G1 (Fig. 2g). Moreover, CDC6 accumulation under conditions of blocked protein synthesis was not further enhanced on proteasome inhibition, suggesting reduced protein turnover of CDC6 (Fig. 2h), possibly also due to reduced activity of APC^{Cdh1}, another E3 ligase that targets CDC6 for degradation[23]. Indeed, abundance of FZR1 (also known as CDH1), the substrate recognition and activating component of the APC was decreased (Fig. 2i). Downregulation of FZR1 contributes to high E2F1 levels (Fig. 2c and Supplementary Fig. 1ci–ii)[24,25], thereby further boosting CDT1 expression[13]. Enhanced CDC6 stability was associated with Cdk2-mediated phosphorylation at Ser54 (CDC6-pS54) that protects CDC6 from degradation (Fig. 2h)[23]. Despite p21-mediated Cdk2 activity decrease (Supplementary Fig. 1ciii), reduction of FZR1 appears to tilt the balance in favour of CDC6 accumulation (total and CDC6-pS54) (Fig. 2h). Notably, protein synthesis and proteasome inhibition did not restore FZR1 protein levels, implying regulation at the transcriptional level, a notion confirmed experimentally (Fig. 2i).

Given that most clinical specimens with p21/Ki67 double-positive cells were p53-deficient, we examined whether p53 impacts the ability of p21 to regulate the CDT1 and CDC6 levels, as previously suggested[26]. Indeed, p21 expression in p53-defective and p53 wild-type (WT p53) cell types resulted in increased (Figs 2c and 3a,d), and suppressed (Fig. 3b,c,e) RLF abundance, respectively. It was suggested that p53 shields the organism from cells undergoing re-replication by triggering apoptosis[26]. Consistently, after p21 induction WT p53 HT1080 p21-IPTG-ON cells experienced massive apoptosis, accompanied by a dramatic decrease of CDT1 and CDC6 (Fig. 3e). Conversely, silencing of p53 suppressed apoptosis and allowed upregulation of CDT1 and CDC6 (Fig. 3e). Similar results were obtained on p53 restoration in the Saos2 cellular system (Fig. 3c)[27].
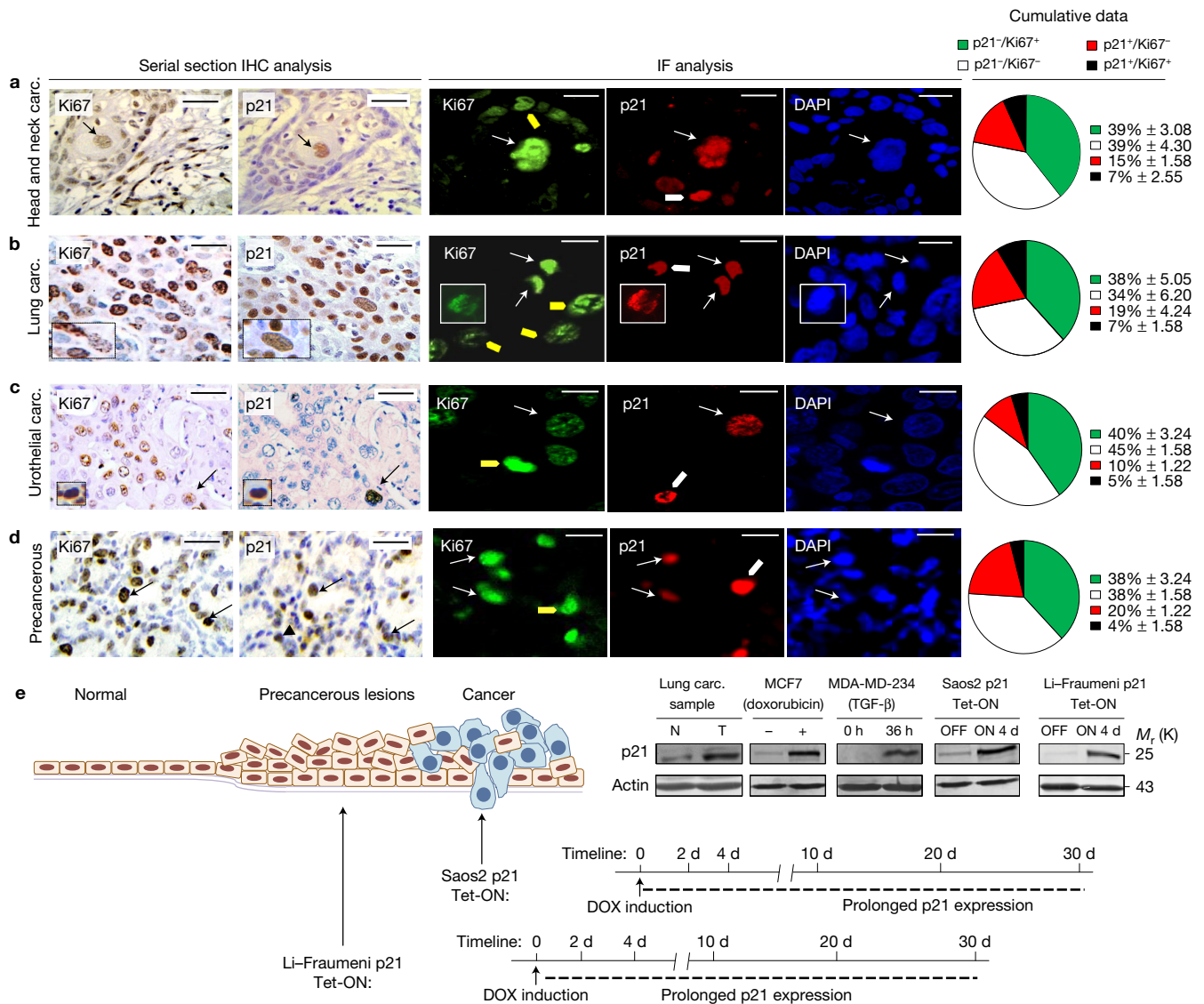
Figure 1 p21 and Ki67 are co-expressed in a subset of atypical cells of high-grade/poorly differentiated, advanced human carcinomas and precancerous lesions. (**a**–**d**) Serial-section immunohistochemical (IHC) analysis and double immunofluorescent (IF) analysis showed co-expression of p21 and the mitotic marker Ki67 in a subset of large cancer cells with giant nuclei in head and neck squamous cell carcinomas (**a**), lung squamous cell carcinomas (inset depicts in higher magnification, a large atypical cell with p21/Ki67 co-expression) (**b**), urothelial carcinomas (**c**) and colon precancerous lesions (dysplasia-associated lesions or masses), obtained from patients with ulcerative colitis, which are known to exhibit early p53 aberrations[17] (**d**). (**e**) Cellular models used to recapitulate the *in vivo* observations. Timeline of p21 induction in Li–Fraumeni p21 Tet-ON and Saos2 p21 Tet-ON cells, showing time points where main biochemical and phenotypical events occur. IHC and IF: black and white thin arrows denote p21 and Ki67 co-expressing cells, respectively; IF: white and yellow thick arrows depict cells with mutually exclusive p21 and Ki67 expression, respectively. Scale bars in IHC panels, 50 μm; IF panels, 50 μm. Unprocessed original scans of blots are shown in Supplementary Fig. 9.

Last, exposure to p53-independent p21-inducing stimuli such as TGF-β led to upregulation of both RLFs (Fig. 3d).

Expression of p21 in p53-null cells triggers replication stress in a CDT1/CDC6-dependent manner

Re-replication is a form of replication stress driven mainly by inappropriate expression of RLFs[6,8,9], leading to DNA damage and DNA damage response (DDR) activation[6,9]. Following p21 induction in both, Saos2 and Li–Fraumeni p21 Tet-ON cellular systems, chromatin loading of the MCM2-7 helicase complex increased robustly, indicating that CDT1 and CDC6 upregulation is functional

(Supplementary Fig. 1d). Flow cytometry analysis of cells double-stained for DNA content and DNA synthesis revealed a cell subpopulation with DNA content greater than 4n, indicative of re-replication (Fig. 3f–h and Supplementary Video 4). Subsequently, DNA damage, assessed by the alkaline comet assay (total number of DNA lesions) and pulsed-field gel electrophoresis (PFGE) was evident and accompanied by DDR, documented by H2AX phosphorylation (γH2AX) and increased 53BP1 foci formation (Fig. 4a–e and Supplementary Fig. 1ei–iv). Strikingly, re-replication, DNA damage and DDR activation were CDC6- and CDT1-dependent, further suggesting that deregulated p21 causes replication stress associated
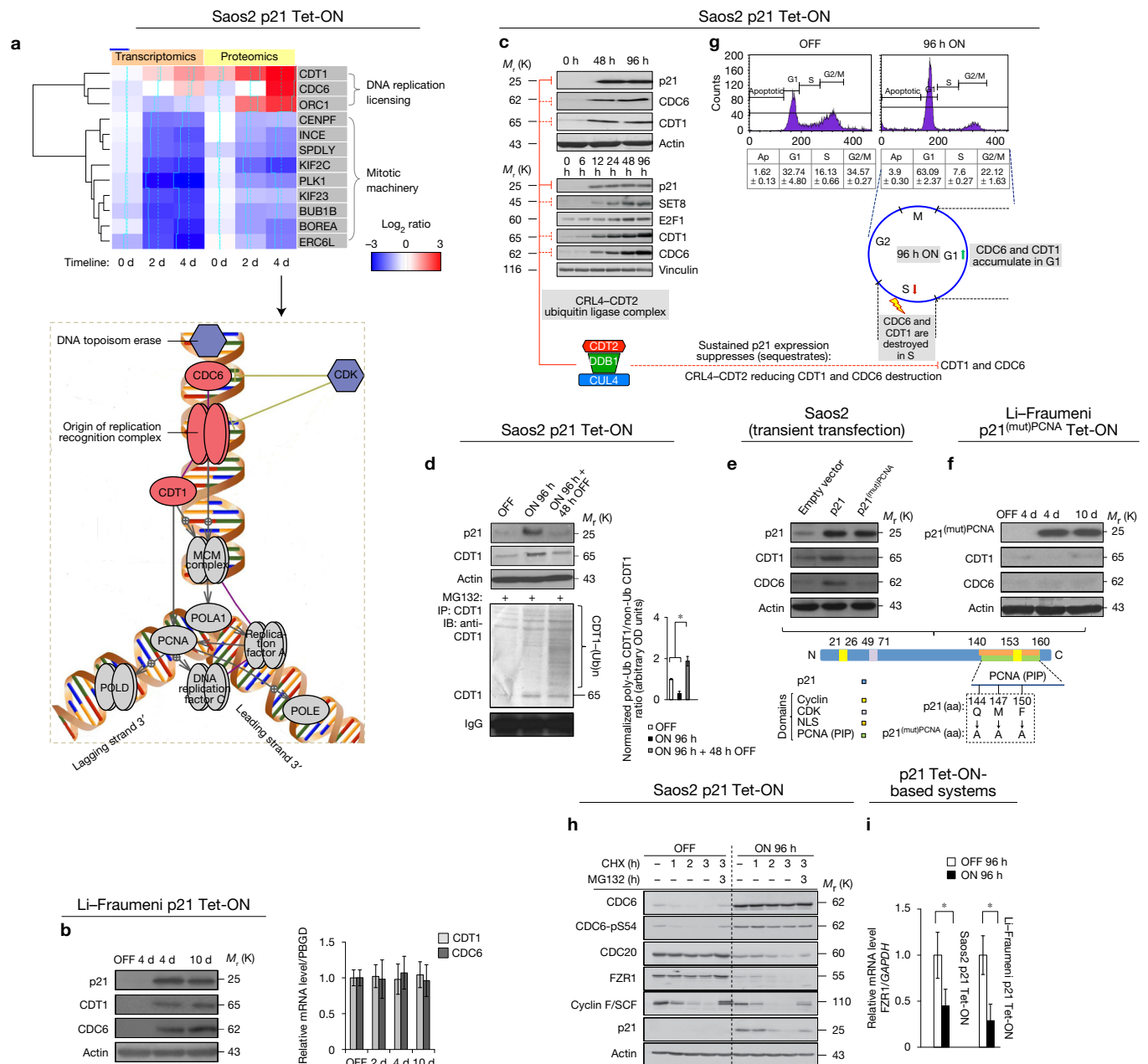
Figure 2 Prolonged stimulation of p21 upregulates and stabilizes the RLFs CDC6 and CDT1 at the protein level. (**a**) Upper panel: heat maps of transcriptomic and proteomic analyses, at days 2 and 4, after p21 induction in Saos2 p21 Tet-ON cells. Sets of significantly overexpressed and underexpressed genes are shown. Lower panel: a schematic representation of significant genes that are upregulated and downregulated, along with their biochemical function, at day 4 of p21 induction. Data derived from three biological replicates (transcriptomics) and two replicates (proteomics) (see Methods). (**b**) p21 induction in Li–Fraumeni p21 Tet-ON cells leads to CDT1 and CDC6 upregulation only at the protein level. Lower panel: real-time RT–PCR performed at the depicted time points showing no changes in transcriptional levels of the same factors ($P =$ not significant, ANOVA, error bars indicate mean ± s.d., $n = 3$ experiments). (**c**) CDT1 stabilization possibly via suppression of the CRL4–CDT2 ubiquitin ligase complex due to overabundance of p21. (**d**) Ubiquitylation-dependent decrease of CDT1 levels following p21 switch-off. Doxycycline-induced Saos2 p21 Tet-ON cells were subsequently shut off for the indicated time points and treated also with 30 μM MG132 (*$P < 0.0001$, ANOVA, error bars indicate

mean ± s.d., $n = 3$ blots). IB, immunoblot. (**e**) Saos2 cells were transfected with wild-type p21 and a specific p21 mutant (p21$^{(mut)PCNA}$: harbouring Gln144, Met147, Phe150 substitutions to alanine in its PCNA-interacting-protein (PIP) degron motif—see panel below) abrogating its interaction with PCNA. (Empty vector: pMSCV, p21: pMSCV–p21, p21$^{(mut)PCNA}$: pMSCV–p21$^{(mut)PCNA}$.) (**f**) Induction of p21$^{(mut)PCNA}$ abrogated upregulation of CDT1 and CDC6 in Li–Fraumeni cells. The panel below **e** and **f** presents p21 protein structure and domains. Location of mutations in the PIP motif of p21$^{(mut)PCNA}$ is also depicted. (**g**) CDT1 and CDC6 reduced turnover due to the cell-cycle profile imposed by constitutive p21 expression. (**h**) Stabilization of CDC6 by p21 overexpression. (**i**) Real-time RT–PCR assessment of FZR1 in induced and non-induced Saos2 and Li–Fraumeni p21 Tet-ON cells (*$P = 0.02108$ (Saos2), *$P = 0.00479$ (Li–Fraumeni), t-test, error bars indicate mean ± s.d., $n = 3$ experiments). Actin and vinculin serve as loading controls; *GAPDH* serves as a normalizing housekeeping gene; h, hours; MG132, proteasome inhibitor; CHX, cycloheximide. Unprocessed original scans of blots are shown in Supplementary Fig. 9. Source data are available in Supplementary Table 25.
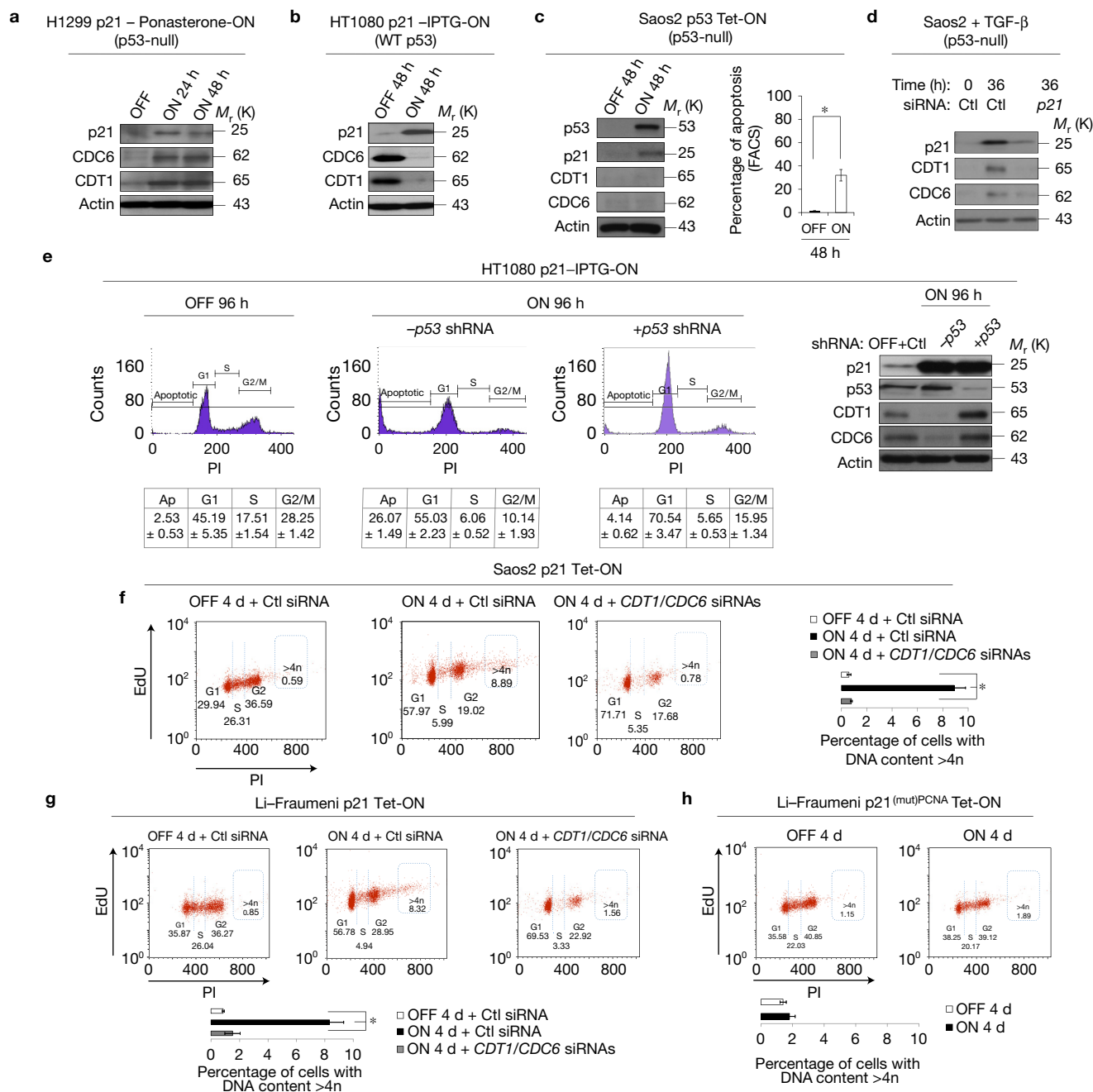
Figure 3 The status of p53 defines the ability of p21 to regulate the levels of CDT1 and CDC6. (**a**,**b**) Immunoblots for CDT1 and CDC6 in H1299 p21–Ponasterone-ON (**a**) and HT1080 p21–IPTG-ON (**b**) cells challenged with p21. (**c**) Immunoblots for CDT1 and CDC6 in Saos2 p53 Tet-ON cells on p53 induction. The histogram illustrates apoptosis as assessed by flow cytometry analysis (FACS) after p53 induction (*$P < 0.01$, t-test, error bars indicate mean ± s.d., $n = 5$ experiments). (**d**) Immunoblots for CDT1 and CDC6 in Saos2 cells treated with TGF-β (see also Supplementary Fig. 1eiii–iv). (**e**) FACS of HT1080 p21–IPTG-ON cells showed that induction of apoptosis as well as CDT1 and CDC6 expression is p53-dependent following p21 expression. Corresponding immunoblots for p53, CDT1 and CDC6 in the manipulated HT1080 p21–IPTG-ON cells. PI, propidium iodide. (**f–h**) FACS analysis of Saos2- (**f**) and Li–Fraumeni-p21 Tet-ON (**g**) cells showed an accumulation of cells with >4n DNA content (re-replication) after p21 induction that is CDT1- and CDC6-dependent (*$P < 0.0001$, ANOVA, error bars indicate mean ± s.d., $n = 5$ experiments). Similar analysis using the p21(mut)PCNA mutant (**h**; see also the panel under Fig. 2e,f) abrogated re-replication (P = not significant, t-test, error bars indicate mean ± s.d., $n = 5$ experiments). Actin serves as a loading control. Ctl, control short-hairpin RNA; d, days; h, hours. Unprocessed original scans of blots are shown in Supplementary Fig. 9. Source data are available in Supplementary Table 25.

with re-replication (Fig. 4b–e). Likewise, silencing of p21 alleviated DNA damage and DDR (Supplementary Figs 1eiii,iv and 2ai–iii). DNA damage reduction was negligible on deoxynucleoside 5′-triphosphate

supplementation, in contrast to the impact of CDT1 and CDC6 silencing (Fig. 4d)[28]. Finally, re-replication and DNA damage were significantly reduced when the p21(mut)PCNA mutant was employed,
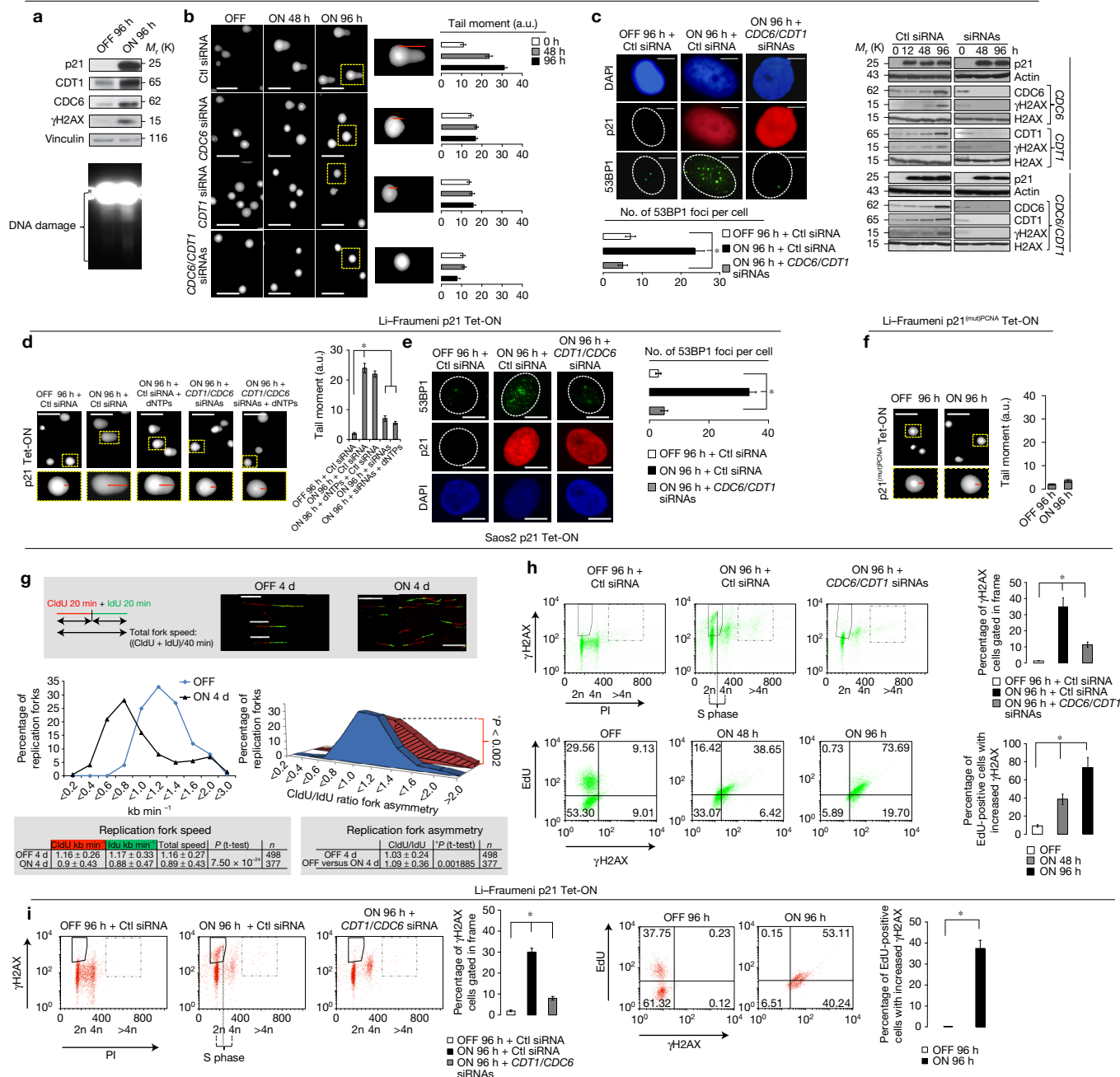
Figure 4 Sustained p21 expression triggers replication stress and DNA damage accumulation in a CDT1/CDC6-dependent manner in S phase. (**a**) PFGE depicts DNA damage on prolonged p21 expression. (**b**) Assessment of DNA breaks with comet assays in Saos2 p21 Tet-ON induced for the indicated time points and after *CDC6* or *CDT1* siRNA silencing or both. Red lines in inset magnifications depict comet (moment) tails. (**c**) p21 expression, in cells with non-functional p53, activated the DDR pathway in a CDC6- and CDT1-dependent manner ($P < 0.0001$, ANOVA, error bars; mean $\pm$ s.d., $n = 3$ experiments). (**d**–**f**) p21-dependent CDC6 and CDT1 overexpression produces DNA damage and activation of the DDR pathway in a CDC6- and CDT1-reliant manner in Li–Fraumeni p21 Tet-ON cells as assessed by comet assay (**d**) and immunofluorescence analysis of DDR markers (**e**). Comet assays using p21 (mut)PCNA demonstrated the absence of DNA damage (**f**). Red lines in inset magnifications label comet (moment) tails. (*$P < 0.0001$, ANOVA (**d**,**e**); $P =$ not significant, *t*-test (**f**); error bars, mean $\pm$ s.d., $n = 3$ experiments.) dNTPs, deoxynucleoside 5′-triphosphates. (**g**) Reduced replication fork speed

and replication fork asymmetry on sustained p21 expression (*$P < 0.001$, $P < 0.002$, *t*-test, $\pm$ indicate s.d., n values represent the number of forks analysed across two experiments). Saos2 p21 Tet-ON non-induced versus induced cells (96 h) after 20 min consecutive labelling pulses of CldU (red) and IdU (green) were subjected to DNA fibre analysis. (**h**,**i**) Protracted p21 expression inflicts DNA damage in S phase in Saos2 p21 Tet-ON (**h**) and Li–Fraumeni p21 Tet-ON cells (**i**). FACS of p21-induced cells for 96 h and co-stained for γH2AX/propidium iodide (PI), with or without anti-*CDC6/CDT1* siRNA targeting, and p21-induced cells for the indicated time points and co-stained for EdU/γH2AX. Histograms for γH2AX/PI depict counts in rectangular areas (both dashed and not) (*$P < 0.0001$, ANOVA and *t*-test respectively, error bars; mean $\pm$ s.d., $n = 5$ experiments). Actin, H2AX and vinculin serve as loading controls; Ctl, control siRNA; d, days; h, hours. Unprocessed original scans of blots are shown in Supplementary Fig. 9. Scale bars, 7.5 μm (**c**,**e**) and 50 μm (**b**,**d**,**f**). Source data are available in Supplementary Table 25.

consistent with our model that excess p21 acts by suppressing PCNA-dependent ubiquitylation of CDT1 and CDC6 (Figs 2f, 3h and 4f and Supplementary Fig. 1ei,ii)[8].

It seems paradoxical that p21 could trigger replication stress, given its role as a potent cell-cycle inhibitor. Nevertheless, DNA combing showed that replication fork progression did not cease, but its speed was reduced (Fig. 4g). In addition, replication fork asymmetry was observed, possibly related to the presence of DNA lesions impeding bi-directional fork movement (Fig. 4g). Consistently, multi-parameter flow cytometry analysis of γH2AX, DNA content and DNA synthesis showed that, following p21 induction, DNA damage accumulated mainly in cells incorporating EdU, whereas depletion of CDC6 and CDT1 profoundly suppressed the accumulation of DNA damage in S phase (Fig. 4h,i). Markedly, the cells expressing p21 demonstrated a focal PCNA pattern typical for early S phase (Supplementary Fig. 2b)[29], suggesting that DNA damage occurs at a sensitive period when particularly active genes and early-replication fragile sites are replicated[30].

p21-induced replication intermediates are processed by MUS81–EME1 and repaired by a Rad52-dependent mechanism

To further characterize p21-induced replication stress, we examined single-stranded DNA (ssDNA) formation, a common intermediate at replication-associated lesions. To this end, p21-expressing cells were incubated with BrdU under non-denaturing conditions, allowing anti-BrdU staining to selectively visualize ssDNA regions[31]. *In situ* analysis showed a strong correlation between the native BrdU staining and p21 expression (Fig. 5a,b) that was also associated with an increased number of foci formed by the ssDNA-binding protein RPA (Fig. 5c). The ssDNA could occur on either the template or the newly synthesized (nascent) strand[32–34]. BrdU staining was absent on short BrdU pulses, suggesting that the source of ssDNA is the template strand (Supplementary Fig. 2c).

Next, we inspected replication intermediates *in vivo* by an established electron microscopy method[35]. Compared with the WT p53 U2OS cell line[36], in unperturbed Saos2 cells we found pronounced accumulation of the so-called reversed forks (Fig. 5di), four-way DNA junctions that have been proposed to limit the amount of exposed ssDNA and thereby possibly mitigate the detrimental impact of gross replication stress[36,37]. Expression of p21 in the Saos2 cell model led to a marked accumulation of small replication bubbles (Fig. 5dii), decreased fork reversal and enhanced accumulation of ssDNA stretches at replication forks, with most small bubbles showing one side entirely single-stranded (hemireplicated) (Fig. 5di,iii). Overall, these data are consistent with the notion that p21 expression in p53-defective cancer cells deregulates origin firing, leading to accumulation of ssDNA and increased replication stress.

Replication intermediates need to be resolved for replication to restart. After long periods of replication inhibition, double-strand breaks generated by the structure-specific resolvase complex of MUS81–EME1 are required for replication restart[32,38]. We hypothesized that sustained p21 expression may phenocopy this state. Indeed, MUS81–EME1 depletion caused a significant DNA damage decrease, inflicted by p21 expression, as well as reduction of EdU-positive cells harbouring signs of DNA damage (Fig. 5e–g

and Supplementary Fig. 2di,ii). MUS81–EME1 is considered a central player in oncogene-induced DNA damage response[39,40], promoting homologous recombination-mediated repair of inactivated (collapsed) forks[32]. Surprisingly, we noticed that silencing of the homologous recombination recombinase Rad51 resulted in decreased γH2AX levels (Fig. 5h). This finding implies a negative control over an alternative, Rad51-independent, repair process. Rad51 seems to exert such an effect preventing Rad52-dependent DNA repair[41]. Indeed, suppression of Rad52 was followed by increased γH2AX and cell death in both p21-induced models (Fig. 5i–k), suggesting that Rad52 guided the repair process. Rad52 is possibly involved in error-prone microhomology-mediated repair pathways challenging genomic stability[42,43]. Interestingly, Rad51 levels were reduced on p21 induction (Fig. 5h and Supplementary Fig. 2diii). Rad51 is in short supply and under stressful conditions, such as hypoxia, *Rad51* is repressed by E2F4/p130 complexes. Such complexes are recruited by p21 to mediate gene repression[44]. In accordance, the promoter of *Rad51* was occupied by E2F4 (Fig. 5l), providing an explanation of why Rad52 is chosen for repair in this setting.

Deregulated CDT1 and CDC6 link p53-independent p21 induction with senescence

Sustained p53-independent p21 expression triggered senescence, a well-established antitumour barrier, in a CDT1- and CDC6-dependent manner (Fig. 6a,b)[14,45]. Consistently, no signs of senescence were observed when the p21(mut)PCNA-inducible mutant was employed or p21 was silenced (Fig. 6c and Supplementary Fig. 2ai–iii). As p73, the p53 homologue, responds to DDR signalling[46], we asked whether p73 could operate downstream in the emerging p21–RLFs–DDR-signalling route. Indeed, p73 proved to be required for the p21-CDT1/CDC6-induced senescence (Fig. 6d,e).

According to the oncogene-induced DNA damage concept for cancer development, the DDR-mediated anti-tumour barriers are breached at some point in tumours that progress, accompanied by genomic instability[12]. If this concept is applicable for chronic p53-independent p21 induction, then in due time the p21-expressing cells could bypass the senescence barrier generating more aggressive outgrowing clones. CDC6 overexpression *per se* could contribute to senescence bypass by repressing the *INK4/ARF* locus[47], encoding p16INK4A, an indispensable factor of irreversible senescence[48]. Indeed, p21 activation led to downregulation of both *INK4/ARF* products, p16INK4A and p14ARF, undermining the durability of p21-mediated senescence (Fig. 6f,g).

Senescence bypass, genomic instability and enhanced aggressiveness under protracted p21 expression

After 10 days of p21 induction in p53-deficient models the senescent phenotype gradually declined and a subpopulation of proliferating p21-positive cells emerged (Fig. 7a–e and Supplementary Video 5). Likewise the mutually exclusive expression pattern of cyclin A—an established late S/G2 marker[49,50]—and p21 was reduced and replaced by a p21/cyclin A double-positive cell subpopulation (Fig. 7f). It appears that a fraction of p21-expressing cells evaded arrest/senescence, re-entering the cell cycle ('escaped cells'). Cdk2 activity and its stimulatory phosphorylation (pT160) were concomitantly restored (Fig. 7g and Supplementary Fig. 2ei). Notably, p21
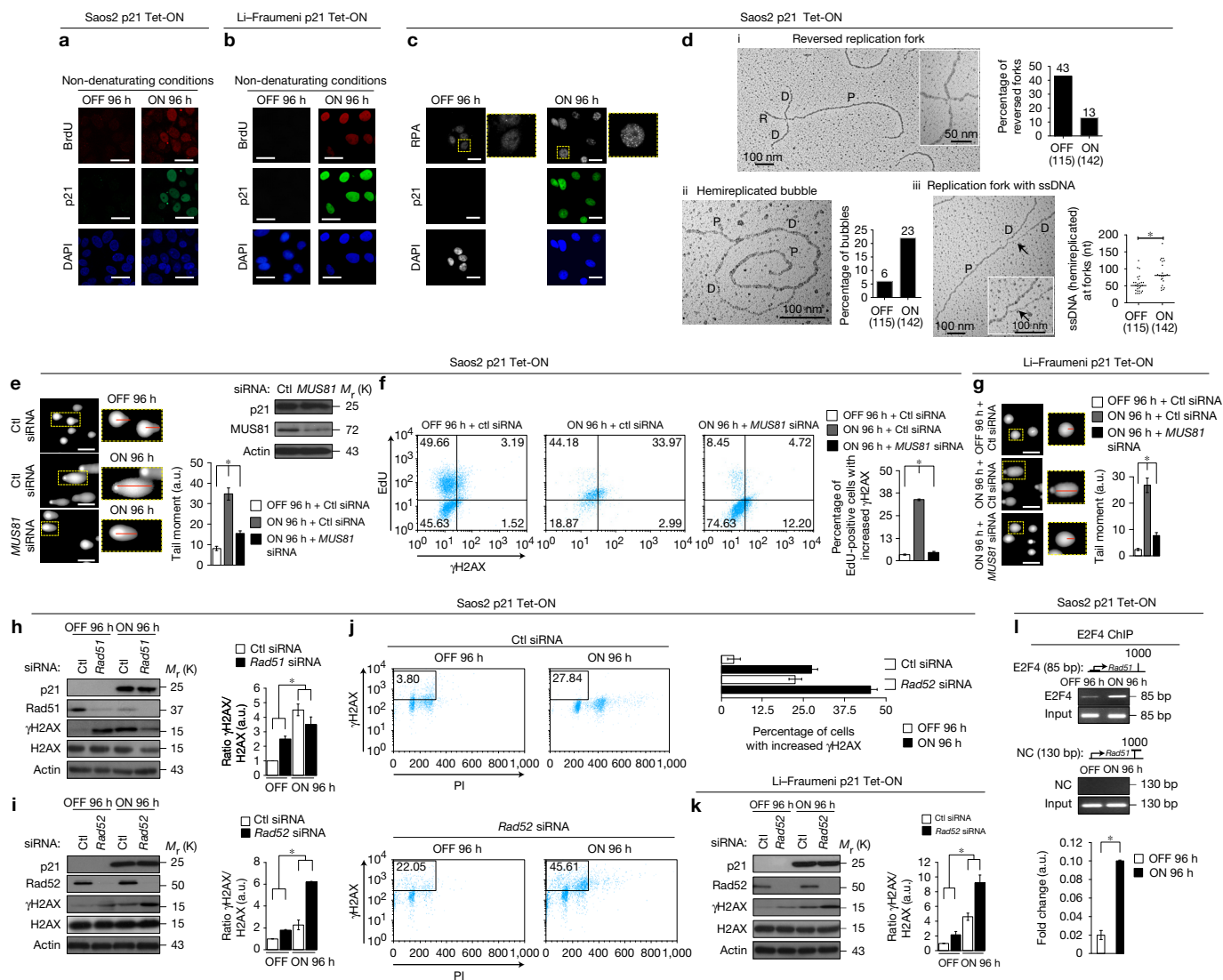
Figure 5 Extended p21 overexpression mediates accumulation of replication intermediate lesions that are processed by MUS81–EME1 and repaired by a Rad52-dependent mechanism. (**a**–**c**) Single-stranded DNA production in p21-overexpressing cells (ON) compared with non-overexpressing cells (OFF). Scale bars, 25 μm. (**d**) (i) Electron micrograph of reversed replication fork from p21-induced Saos2 cells. Histogram depicts frequency of reversed replication forks. The numbers in brackets denote the total number of analysed molecules; the numbers above each column indicate the percentage of reversed forks. (ii) Electron micrograph of a replication bubble with one side entirely single-stranded in p21-induced Saos2 cells. Scale bar, 100 nm. The histogram depicts frequency of replication bubbles (brackets: total number of analysed molecules; above each column: percentage of replication bubbles). (iii) Electron micrograph of a replication fork in p21-induced Saos2 cells. Black arrow, ssDNA region. Graphical distribution of ssDNA length at the junction (black arrow) in Saos2 p21 Tet-ON and OFF cells. Only molecules with detectable ssDNA stretches are included. The lines show the median lengths of ssDNA regions at the fork in the specific set of analysed molecules (*$P \leq 0.001$; Mann–Whitney test) (the numbers in brackets denote the total number of analysed molecules) (P, parental duplex; D, daughter duplexes; R, regressed arm). (**e**–**g**) p21-mediated DNA damage is processed by MUS81 resolvase (*$P < 0.0001$, ANOVA). Red lines in insets, comet (moment) tails; scale bars, 50 μm (**e**,**g**). FACS of Saos2 p21 Tet-ON induced cells for 96 h and co-stained for EdU/γH2AX, with or without anti-*MUS81* silencing (**f**). (**h**) Silencing of *Rad51* resulted in decreased γH2AX levels (*$P < 0.01$, *t*-test). (**i**–**k**) Suppression of *Rad52* was followed by increased γH2AX expression and cell death (*$P < 0.0001$, ANOVA), as shown by immunoblots (**i**,**k**) and FACS analysis (**j**). (**l**) The *Rad51* promoter is occupied by E2F4 on p21 induction as assessed by chromatin immunoprecipitation (ChIP) (*$P < 0.000913$, *t*-test). Actin and H2AX, loading controls; Ctl, control siRNA; h, hours. Unprocessed original scans of blots are shown in Supplementary Fig. 9. Error bars indicate mean ± s.d., $n = 3$ experiments in comet assays (**e**,**g**), blots (**h**,**i**,**k**) and ChIP (**l**); $n = 5$ experiments for FACS analyses (**f**,**j**). Source data are available in Supplementary Table 25.

expression in the 'escaped' cells was similar to, or even higher than, that observed in the initial phase of p21 induction, excluding the possibility that low p21 stoichiometric concentrations drive proliferation (Fig. 7g and Supplementary Fig. 2eii,iii)[1]. The 'escaped' cells showed a dramatic reduction of p73 expression (Fig. 7g,h). There

was no evidence of genetic or epigenetic inactivation of the *p73* locus but instead downregulation of EGR1, the main transcriptional activator of *TP73* (Supplementary Figs 2f and 3–5)[51]. The nuclei in most 'escaped' cells were larger than those in the cycling control cells (Fig. 7i and Supplementary Video 5), a feature noticed also
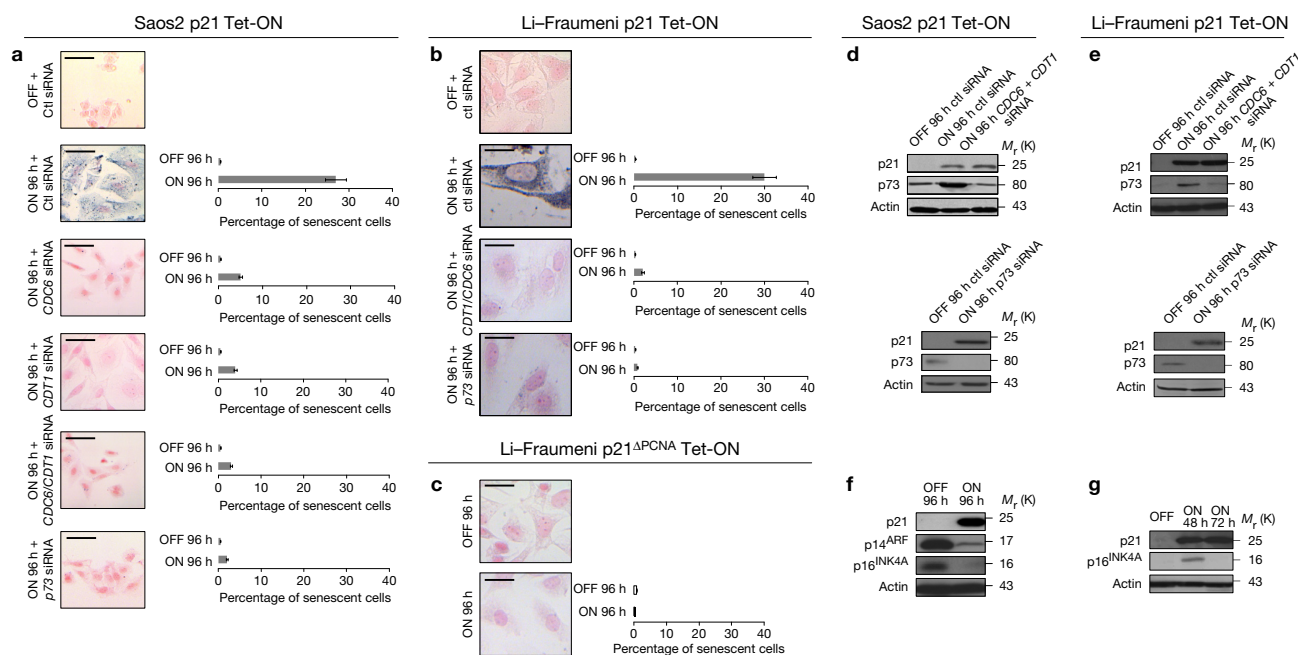
Figure 6 Deregulated upregulation of CDC6/CDT1 links p53-independent activation of p21 with senescence. (**a–c**) Sustained p21 expression triggers senescence in Saos2 p21 Tet-ON (**a**) (scale bars, $20\,\mu$m) and Li–Fraumeni p21 Tet-ON (**b**) cells (scale bars, $10\,\mu$m). (**c**) Induction of p21$^{(mut)PCNA}$ expression in Li–Fraumeni cells does not yield similar results. Cells grown on coverslips were stained to assess the senescent phenotype applying the Sudan Black B protocol and SA-β-gal[66] (scale bars, $10\,\mu$m). (**d,e**) Immunoblots depict p73 status following siRNAs targeting *CDC6* and *CDT1*, as well as the efficiency of anti-*p73* treatment in Saos2 p21 Tet-ON (**d**) and Li–Fraumeni p21 Tet-ON (**e**) cells. (**f,g**) Sustained p21 expression reduces p14^{ARF} and p16^{INK4A} protein levels in Saos2 p21 Tet-ON (**f**) and Li–Fraumeni p21 Tet-ON (**g**) cells. Actin serves as loading control; Ctl, control siRNA; h, hours. Error bars; mean $\pm$ s.d., $n = 3$ experiments. Unprocessed original scans of blots are shown in Supplementary Fig. 9. Source data are available in Supplementary Table 25.

in vivo (Figs 1 and 7j and Supplementary Fig. 2g). Noticeably, *in vivo*, the cells displaying Ki67/p21 co-expression were also CDC6 and/or CDT1 positive (Fig. 7j and Supplementary Fig. 2g). DNA damage was also reduced in the 'escaped' cells, implying that a repair process took place (Fig. 7k). The involvement of the MUS81–EME1–Rad52 repair route (Fig. 5e–k) and the increased presence of micronuclei (Fig. 8a) that are considered surrogate markers of chromosomal instability, defective DDR and repair[52] indicated that such repair was error-prone. To gain a genome-wide view of this emerging scenario we performed array comparative genomic hybridization (aCGH), deep sequencing and multicolour fluorescence *in situ* hybridization/spectral karyotyping (M-FISH/SKY) comparing the 'escaped' and the non-induced cells (Fig. 8 and Supplementary Figs 4–6 and Supplementary Tables 10–12). Cumulatively, the results from six independent biological replicates employing all three experimental procedures showed that the genomic landscape of the 'escaped' cells acquired chromosomal aberrations, in the form of gains and losses (Fig. 8b,c and Supplementary Figs 4a–c, 5 and 6 and Supplementary Tables 10–12), as well as novel translocations (Fig. 8d–f and Supplementary Fig. 4c and Supplementary Tables 13–15). Notably, a high frequency of microhomologies ($\geq$2 nucleotides)[42] was identified adjacent to the novel breakpoints in both systems, favouring a role of microhomology-mediated repair in p21-driven genomic instability (Fig. 8d,e and Supplementary Fig. 7 and Supplementary Table 16). Interestingly, among the genetic lesions found were alterations reminiscent of chromoanasynthesis or chromothripsis (Fig. 8b,c and Supplementary Tables 10 and 11)[53]. Given that the multifaceted

chromosomal assessment showed concordant results (Fig. 8d–g and Supplementary Figs 4–6) and each experimental procedure took place at different time periods, we propose that p21 may steer a 'deterministic' set of genetic events that may play a role in the behaviour of the 'escaped' cells. In line with this notion the transcriptome of the 'escaped' cells (Supplementary Figs 3 and 8) demonstrated a specific nonrandom correlation with the genomic alterations found in these cells ($P < 2.2 \times 10^{-16}$ for the Saos2 and $P = 0.0013$ for the Li–Fraumeni cells). Deregulation of the replication licensing machinery was the earliest biochemical event observed on p21 induction, further suggesting that genomic instability 'drove' the alterations in transcriptome landscapes of the 'escaped' cells. While p21 is not a transcription factor it can modulate transcription in certain cases[54]. However, the fact that only 42 (7.6%) of the 553 genes and 538 (15%) of the 3,507 genes found differentially expressed in the 'escaped' Saos2 and Li–Fraumeni p21 Tet-ON cells, respectively, were detected in earlier time points makes the scenario of more 'direct' transcriptional effects of p21 most unlikely (Supplementary Fig. 8).

Importantly the 'escaped' clones demonstrated enhanced anchorage-independent growth and were more invasive (Fig. 8h,i,l). Furthermore, they tolerated treatment with the genotoxic drugs doxorubicin and cisplatin much more efficiently, yet showed no significant difference in the response to taxol, a microtubule polymer stabilizer. The enhanced resistance to doxorubicin and cisplatin persisted even when p21 was switched off in the 'escaped' cells for 10 days, documenting that this feature was a durable consequence, independent of any potential p21-mediated transient
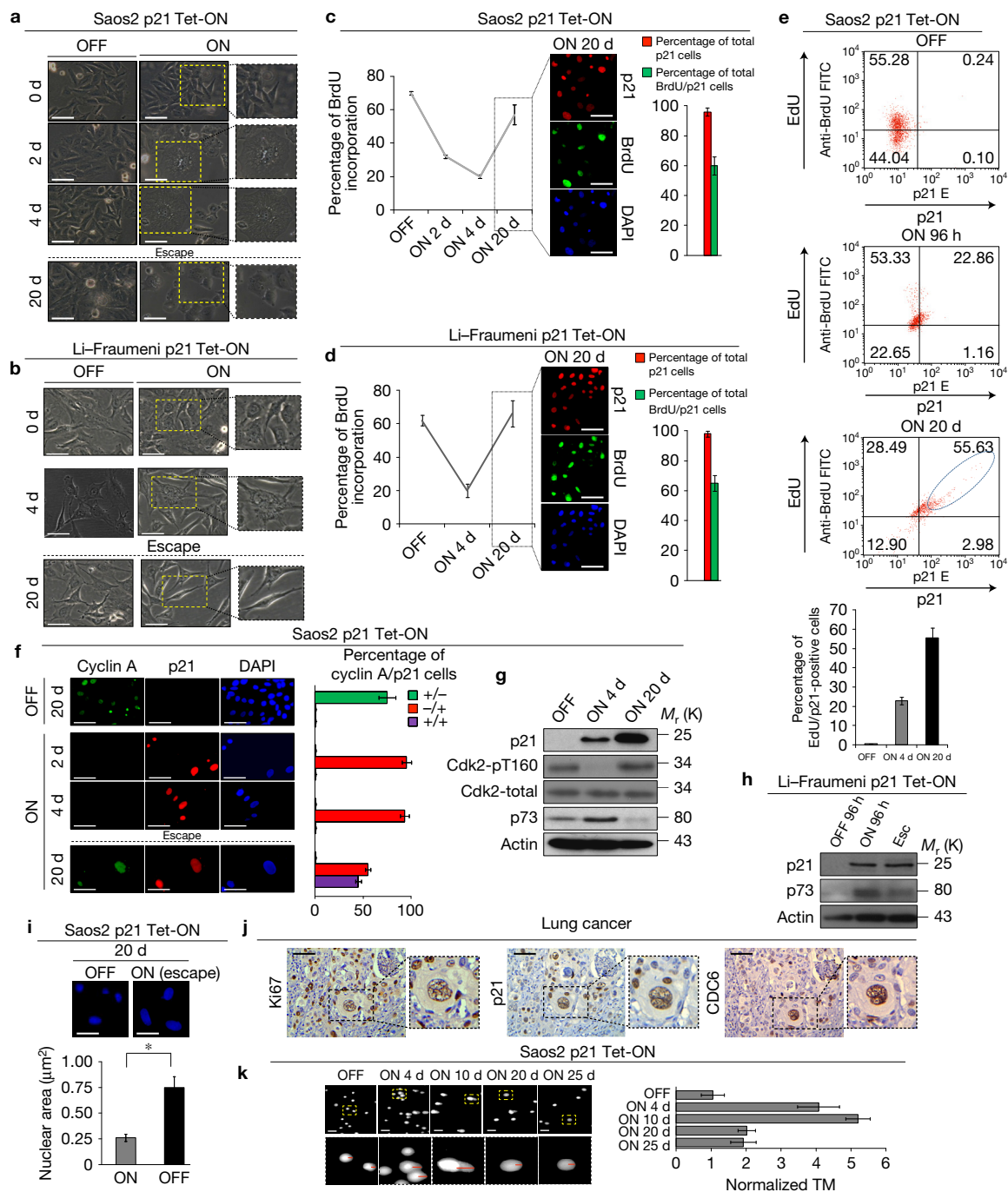
Figure 7 Prolonged p21 expression, in cells with p53 loss of function, overrides the senescence barrier. (**a,b**) Morphological features observed by inverted-phase contrast microscopy of escaped cells (20 days of p21 expression) in Saos2 p21 Tet-ON (**a**) and Li–Fraumeni p21 Tet-ON (**b**) cells. Scale bars, 15 μm. (**c,d**) BrdU incorporation is restored to almost similar levels to non-induced cells after bypass of senescence in Saos2 p21 Tet-ON (**c**) and Li–Fraumeni p21 Tet-ON (**d**) cells (error bars indicate mean ± s.d., $n = 3$ experiments). Scale bars, 50 μm. (**e**) EdU incorporation increases in p21-expressing cells after 20 days of continuous induction (error bars indicate mean ± s.d., $n = 5$ experiments). (**f**) Appearance of a significant subpopulation of cyclin A- and p21-positive cells at 20 days of induction. Double IF analysis of induced cells for cyclin A and p21 at the indicated time points (error bars indicate mean ± s.d., $n = 3$ experiments). Scale bars, 50 μm. (**g,h**) Restoration of Cdk2 activity and reduction of p73 levels (Saos2 p21 Tet-ON (**g**) and Li–Fraumeni p21 Tet-ON (**h**) cells) in cells 'escaping' senescence (see also Supplementary Fig. 2e). (**i**) Escaped cells have larger nuclei than non-induced ones (staining with DAPI). The histogram depicts average values in the OFF versus ON groups, after 20 days (*$P < 0.0001$, t-test, error bars indicate mean ± s.d., $n = 3$ experiments). Scale bars, 7.5 μm. (**j**) Serial-section immunohistochemical (IHC) analysis showed co-expression of p21, Ki67 and CDC6 in atypical cancer cells in clinical samples (see also Supplementary Fig. 2g). Scale bars, 50 μm. (**k**) DNA damage was significantly reduced in escaped cells. Comet assays showed DNA breaks in cells induced for the indicated time points (error bars indicate mean ± s.d., $n = 3$ experiments). Red lines in magnifications of insets label comet (moment) tails (TM) for length comparison. Scale bars, 50 μm. Actin serves as loading control; h, hours. Unprocessed original scans of blots are shown in Supplementary Fig. 9. Source data are available in Supplementary Table 25.
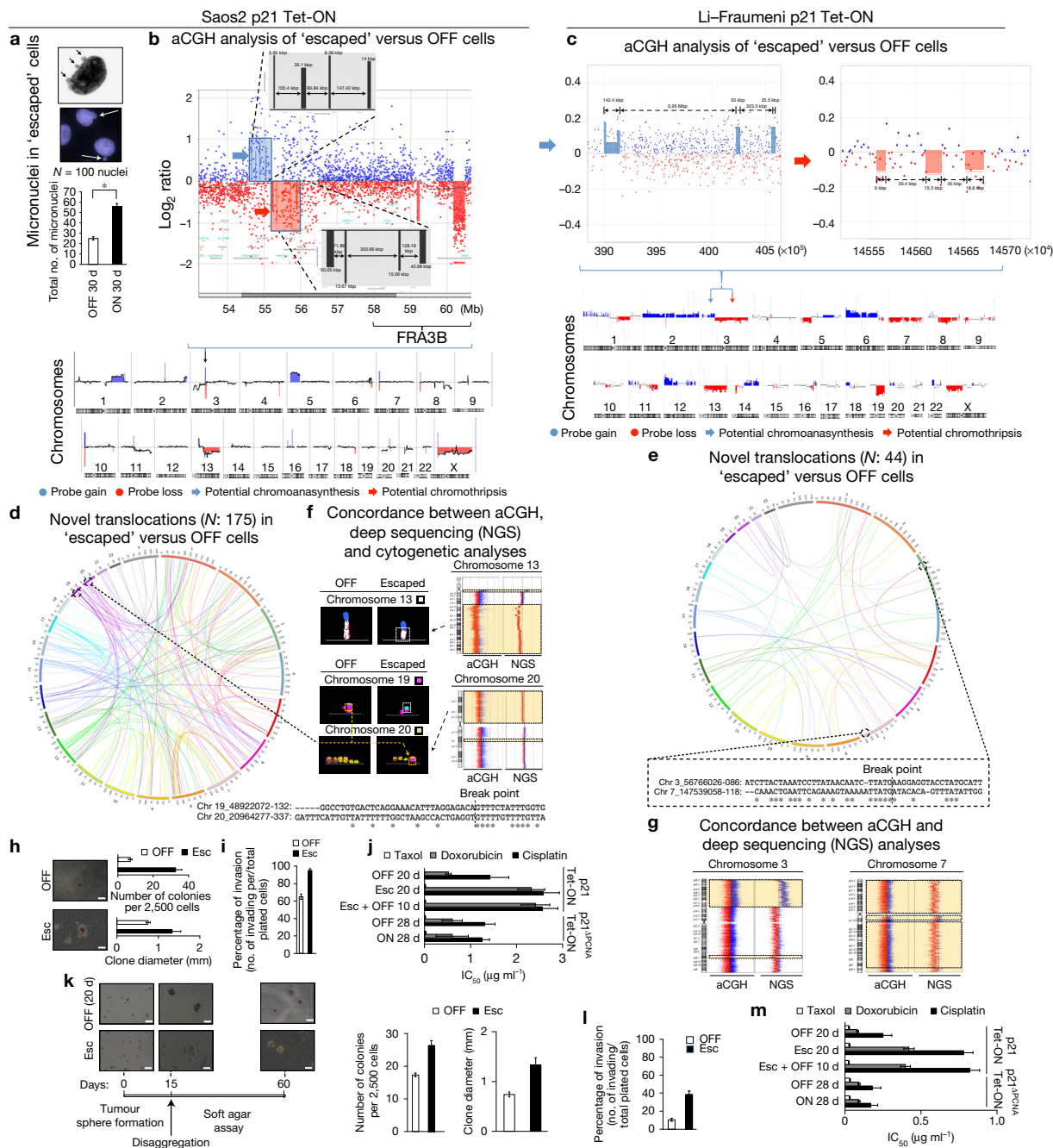
Figure 8 p21-expressing cells that have overridden (escaped) the senescence barrier demonstrate genomic instability and aggressive behaviour. (**a**) Increased frequency of micronuclei in 'escaped' cells. Arrows depict micronuclei (*$P = 0.0098$, t-test, error bars indicate mean ± s.d., $n = 3$ experiments). (**b,c**) High-resolution aCGH analysis between 'escaped' p21-expressing Saos2- (**b**) and Li–Fraumeni-p21 Tet-ON (**c**) cells and non-induced ones at 30 days. Blue and red coloured regions along the chromosome ideograms depict genome gains and losses, respectively. Upper insets (**b,c**) depict narrow subchromosomal areas exhibiting alternating regions of gains or losses with retention regions in between (in blue and red shadowed rectangles, respectively), possibly indicating events of chromoanasynthesis and chromothripsis, respectively. (**d,e**) Circos diagrams depicting novel (**d**, 175; **e**, 44) chromosomal rearrangements in 'escaped' Saos2 (**d**) and Li–Fraumeni (**e**) p21 Tet-ON-expressing cells, respectively, revealed by whole-genome sequencing (human chromosomes are located at the perimeter). A representative breakpoint is also shown. (**f,g**) Representative results showing the high correlation between the aCGH, next-generation sequencing and cytogenetic analyses in 'escaped' p21 cells. Dashed white rectangles; gains or losses, yellow rectangles; translocations. (**h–j**) Escaped Saos2 p21 Tet-ON cells (45 days of p21 expression) form more and larger colonies than cells with non-induced (OFF) p21 in soft agar assay (**h**), display invasion capability (**i**), and exhibit increased genotoxic drug tolerance (**j**). ($P = 0.00373$, $P = 0.034$, $P = 0.000314$ (**h,i**), t-test; $P = 0.91$, $P < 0.0001$, $P = 0.013$ (**j**), ANOVA; error bars indicate mean ± s.d., $n = 3$ experiments). Histogram depicting increased IC_{50} values by escaped cells following treatment with doxorubicin and cisplatin (**j**). (**k**) Escaped Saos2 p21 Tet-ON cells (20 d) demonstrate cancer-stem-cell-like traits as assessed by tumour sphere formation assay coupled to soft agar growth ($P = 0.0045$, $P = 0.0151$, t-test, error bars indicate mean ± s.d., $n = 3$ experiments). (**l,m**) Escaped Li–Fraumeni-p21 Tet-ON cells (45 days of p21 expression) also display invasion capability and increased genotoxic drug tolerance ($P = 0.0015$ (**l**), t-test; $P = 0.38$, $P = 0.0005$, $P = 0.0001$ (**m**), ANOVA; error bars indicate mean ± s.d., $n = 3$ experiments). Source data are available in Supplementary Table 25.

transcriptional effect (Fig. 8j,m). This chemoresistance effect was absent when p21 was silenced very early after p21 induction (Supplementary Fig. 2ai–iii). A number of the transcriptionally altered genes connected with aggressive behaviour could help interpret the acquired aggressive phenotypic features (Supplementary Fig. 3d,e and Supplementary Tables 17–22). Furthermore, assessments of tumour sphere formation and anchorage-independent growth indicated that the 'escaped' populations are enriched in cells with 'stemness'-like features (Fig. 8k and Supplementary Fig. 3d).

DISCUSSION

The present data set demonstrates an unexpected p21-mediated oncogenic mechanism that is distinct from that reported for leukaemia stem cells[55]. It also explains why p21 is only transiently expressed during induction of senescence[48,56] and how p53 inactivation can tip the balance towards the oncogenic function of p21.

When free from the influence of WT p53, p21 induced by p53-independent signals causes deregulation of the replication licensing machinery triggering replication stress. We provide evidence that continuous production of p21 suppresses its degradation module, CRL4–CDT2, possibly by oversaturating it as p21 has the strongest PCNA-binding affinity (Supplementary Fig. 8c)[22], thereby leaving their other targets, including CDT1, CDC6 and E2F1, unabated to perform their functions (Supplementary Fig. 8c). Since CDT1 expression is positively regulated by E2F1 (ref. 13), such a feed-forward mechanism could further boost CDT1 expression (Supplementary Fig. 8c). Although CRL4–CDT2 seems to be the key player in this process, SCF[Skp2], which also targets p21 and CDT1, may also contribute[1,22,57].

By upregulating the pivotal replication licensing factors CDT1 and CDC6, the cells expressing p21 acquire the capacity to re-replicate (or 'endo-reduplicate'), a phenomenon that we now explain mechanistically[58]. We show that p21-mediated genome re-replication eventually drives a chromosome-destabilizing process giving rise to descendant cells with more aggressive cancerous features (Supplementary Fig. 8c). Re-replication is a form of replication stress that leads to replication fork stalling, collapse, DNA damage and eventually genomic instability[8,9,59]. Within this context, the p53 checkpoint was shown to limit re-replication, via eliminating re-replicating cells by apoptosis (Fig. 3b)[26]. The fact that the turnover of p21, CDT1 and CDC6 is controlled by the same E3-ubiquitin ligase, CRL4–CDT2, underscores the significance of p53 whose inactivation abolishes a cell-protective mechanism. Given that *p21* mutations are extremely rare events in cancer[1,5], it is apparent that human cancers with mutant p53 are at risk of suffering additional deleterious, tumour heterogeneity-promoting genetic alterations by protracted operation of p21, induced through p53-independent signals (Supplementary Fig. 1eiii,iv)[1].

The ensuing involvement of MUS81–EME1 and the recombinase Rad52 point towards a replication-based error-prone DNA repair process[39,40]. Reduction of Rad51 elicits a switch from high-fidelity homologous recombination to a lower-fidelity repair process mediated by Rad52 that requires much less homology (microhomology) (Supplementary Fig. 8c)[41,42,60]. The altered genomic landscape and the high frequency of microhomologies found within and adjacent to the mapped breakpoints supports this scenario (Supplementary Figs 4–7). Among the chromosomal aberrations observed, chromoanasynthesis results from replicative template-switching events (Fig. 8b,c)[61].

However, chromothripsis, another complex chromosomal rearrangement pattern noticed here (Fig. 8b,c), is considered to be the outcome of non-homologous end joining[62], implying that other repair pathways, possibly non-replicative ones, may also contribute to the p21-driven genomic instability.

A question that always emerges is whether genomic alterations represent a passenger or a driver event. The strong correlation between the transcriptome and genome changes supports the latter possibility. Among the transcripts found deranged were growth factors and metalloproteinases that could account for the aggressive behaviour of the 'escaped' cells (Supplementary Fig. 3 and Supplementary Tables 17–22). Notably, ID1, shown to antagonize the suppressive effects of p16[INK4A] and p21 (ref. 63), was upregulated in the 'escaped' cells (Supplementary Fig. 3).

Collectively, p21-driven genomic instability constitutes part of a selection trajectory to promote survival and long-term cancer evolution[64], as illustrated mainly by the increased aggressiveness and resistance of the 'escaped' cells to genotoxic agents. This tumour evolutionary scenario involves a combination of p53 defects permissible for passage through a reversible senescence phase (Fig. 6f,g)[48,57] that 'conceals' an underlying replication stress-based/error-prone repair route that over time ensures that the 'fittest and more adapted cancer cells' emerge[10]. Our results highlight the 'dark side' of p21 that should be taken into consideration when designing therapeutic strategies, particularly for p53-deficient tumours, as agents used in clinical oncology, such as dexamethasone, can induce p21 in a p53-independent manner with potential detrimental effects to patients[65]. □

METHODS

Methods, including statements of data availability and any associated accession codes and references, are available in the online version of this paper.

AUTHOR CONTRIBUTIONS
P.G., K.V. and D.W.: cell culture and manipulations, siRNA/plasmid/viral transfections/transductions/infections, immunoblots, cell growth, RT–PCR, ChIP, comet, IHC and IF assays. D.W. and C.S.S.: PFGE analysis. A.M.-M. and J.B.: DNA fibre spreading assay. A.K.A., R.Z., S.H. and M.L.: electron microscopy and cell culture for electron microscopy. E.J.H. and J.J.B.: FACS analyses. B.C., A.I. and A.N.: time-lapse video analyses. D.K.: MTT, soft agar, invasion and kinase assays. F.-M.R. and S.G.: molecular cytogenetic analyses. A.P., A.K. and D.T.: whole-genome and RNA sequencing. M.T. and E.K.: aCGH analyses. K.V., S.D.G.

and P.T.: proteomic analysis. I.B.R.: data analysis and cell line production. K.V. and A.P.: transcriptomic and bioinformatic analyses. J.J.B., C.S.S., A.N. and J.B.: data analysis and interpretation, and assistance in manuscript preparation. V.G.G.: experimental design, guidance, manuscript preparation and writing.

1. Abbas, T. & Dutta, A. p21 in cancer: intricate networks and multiple activities. *Nat. Rev. Cancer* **9,** 400–414 (2009).
2. Roninson, I. B. Oncogenic functions of tumour suppressor p21(Waf1/Cip1/Sdi1): association with cell senescence and tumour-promoting activities of stromal fibroblasts. *Cancer Lett.* **179,** 1–14 (2002).
3. Pateras, I. S., Apostolopoulou, K., Niforou, K., Kotsinas, A. & Gorgoulis, V. G. p57KIP2: "Kip"ing the cell under control. *Mol. Cancer Res.* **7,** 1902–1919 (2009).
4. Rivlin, N., Brosh, R., Oren, M. & Rotter, V. Mutations in the p53 tumor suppressor gene: important milestones at the various steps of tumorigenesis. *Genes Cancer* **2,** 466–474 (2011).
5. Warfel, N. A. & El-Deiry, W. S. p21WAF1 and tumourigenesis: 20 years after. *Curr. Opin. Oncol.* **25,** 52–58 (2013).
6. Abbas, T., Keaton, M. A. & Dutta, A. Genomic instability in cancer. *Cold Spring Harb. Perspect. Biol.* **5,** a012914 (2013).
7. Blow, J. J. & Dutta, A. Preventing re-replication of chromosomal DNA. *Nat. Rev. Mol. Cell Biol.* **6,** 476–486 (2005).
8. Petrakis, T. G. *et al.* Exploring and exploiting the systemic effects of deregulated replication licensing. *Semin. Cancer Biol.* **37–38,** 3–15 (2016).
9. Blow, J. J. & Gillespie, P. J. Replication licensing and cancer—a fatal entanglement? *Nat. Rev. Cancer* **8,** 799–806 (2008).
10. Negrini, S., Gorgoulis, V. G. & Halazonetis, T. D. Genomic instability—an evolving hallmark of cancer. *Nat. Rev. Mol. Cell Biol.* **11,** 220–228 (2010).
11. Halazonetis, T. D., Gorgoulis, V. G. & Bartek, J. An oncogene-induced DNA damage model for cancer development. *Science* **319,** 1352–1355 (2008).
12. Sideridou, M. *et al.* Cdc6 expression represses E-cadherin transcription and activates adjacent replication origins. *J. Cell Biol.* **195,** 1123–1140 (2011).
13. Karakaidos, P. *et al.* Overexpression of the replication licensing regulators hCdt1 and hCdc6 characterizes a subset of non-small-cell lung carcinomas: synergistic effect with mutant p53 on tumor growth and chromosomal instability-evidence of E2F-1 transcriptional control over hCdt1. *Am. J. Pathol.* **165,** 1351–1365 (2004).
14. Liontos, M. *et al.* Deregulated overexpression of hCdt1 and hCdc6 promotes malignant behavior. *Cancer Res.* **67,** 10899–10909 (2007).
15. Rosai, J. R. *Ackerman's Surgical Pathology* (Elsevier, 2011).
16. Velimezi, G. *et al.* Functional interplay between the DNA-damage-response kinase ATM and ARF tumour suppressor protein in human cancer. *Nat. Cell Biol.* **15,** 967–977 (2013).
17. Cooks, T. *et al.* Mutant p53 prolongs NF-κB activation and promotes chronic inflammation and inflammation-associated colorectal cancer. *Cancer Cell* **23,** 634–646 (2013).
18. Agarwal, M. L., Agarwal, A., Taylor, W. R. & Stark, G. R. p53 controls both the G2/M and the G1 cell cycle checkpoints and mediates reversible growth arrest in human fibroblasts. *Proc. Natl Acad. Sci. USA* **92,** 8493–8497 (1995).
19. Bates, S., Ryan, K. M., Phillips, A. C. & Vousden, K. H. Cell cycle arrest and DNA endoreduplication following p21Waf1/Cip1 expression. *Oncogene* **17,** 1691–1703 (1998).
20. Havens, C. G. & Walter, J. C. Mechanism of CRL4(Cdt2), a PCNA-dependent E3 ubiquitin ligase. *Genes Dev.* **25,** 1568–1582 (2011).
21. Jørgensen, S. *et al.* SET8 is degraded via PCNA-coupled CRL4(CDT2) ubiquitylation in S phase and after UV irradiation. *J. Cell Biol.* **192,** 43–54 (2011).
22. Gibbs, E. *et al.* The influence of the proliferating cell nuclear antigen-interacting domain of p21(CIP1) on DNA synthesis catalyzed by the human and *Saccharomyces cerevisiae* polymerase delta holoenzymes. *J. Biol. Chem.* **272,** 2373–2381 (1997).
23. Duursma, A. & Agami, R. p53-dependent regulation of Cdc6 protein stability controls cellular proliferation. *Mol. Cell. Biol.* **25,** 6937–6947 (2005).
24. Peart, M. J. *et al.* APC/C(Cdc20) targets E2F1 for degradation in prometaphase. *Cell Cycle* **9,** 3956–3964 (2010).
25. Budhavarapu, V. N. *et al.* Regulation of E2F1 by APC/C Cdh1 via K11 linkage-specific ubiquitin chain formation. *Cell Cycle* **11,** 2030–2038 (2012).
26. Vaziri, C. *et al.* A p53-dependent checkpoint pathway prevents rereplication. *Mol. Cell* **11,** 997–1008 (2003).
27. Gorgoulis, V. G. *et al.* p53 activates ICAM-1 (CD54) expression in an NF-κB-independent manner. *EMBO J.* **22,** 1567–1578 (2003).
28. Bester, A. C. *et al.* Nucleotide deficiency promotes genomic instability in early stages of cancer development. *Cell* **145,** 435–446 (2011).
29. Essers, J. *et al.* Nuclear dynamics of PCNA in DNA replication and repair. *Mol. Cell. Biol.* **25,** 9350–9359 (2005).
30. Barlow, J. H. *et al.* Identification of early replicating fragile sites that contribute to genome instability. *Cell* **152,** 620–632 (2013).
31. Beck, H. *et al.* Regulators of cyclin-dependent kinases are crucial for maintaining genome integrity in S phase. *J. Cell Biol.* **188,** 629–638 (2010).
32. Petermann, E. & Helleday, T. Pathways of mammalian replication fork restart. *Nat. Rev. Mol. Cell Biol.* **11,** 683–687 (2010).
33. Neelsen, K. J. Deregulated origin licensing leads to chromosomal breaks by rereplication of a gapped DNA template. *Genes Dev.* **27,** 2537–2542 (2013).
34. Couch, F. B. *et al.* ATR phosphorylates SMARCAL1 to prevent replication fork collapse. *Genes Dev.* **27,** 1610–1623 (2013).
35. Neelsen, K. J. *et al.* Visualization and interpretation of eukaryotic DNA replication intermediates *in vivo* by electron microscopy. *Methods Mol. Biol.* **1094,** 177–208 (2014).
36. Zellweger, R. *et al.* Rad51-mediated replication fork reversal is a global response to genotoxic treatments in human cells. *J. Cell Biol.* **208,** 563–579 (2015).
37. Neelsen, K. J. & Lopes, M. Replication fork reversal in eukaryotes: from dead end to dynamic response. *Nat. Rev. Mol. Cell Biol.* **16,** 207–220 (2015).
38. Hanada, K. *et al.* The structure-specific endonuclease Mus81 contributes to replication restart by generating double-strand DNA breaks. *Nat. Struct. Mol. Biol.* **14,** 1096–1104 (2007).
39. Neelsen, K. J., Zanini, I. M., Herrador, R. & Lopes, M. Oncogenes induce genotoxic stress by mitotic processing of unusual replication intermediates. *J. Cell Biol.* **200,** 699–708 (2013).
40. Murfuni, I. *et al.* The WRN and MUS81 proteins limit cell death and genome instability following oncogene activation. *Oncogene* **32,** 610–620 (2013).
41. Wu, Y., Kantake, N., Sugiyama, T. & Kowalczykowski, S. C. Rad51 protein controls Rad52-mediated DNA annealing. *J. Biol. Chem.* **283,** 14883–14892 (2008).
42. Ottaviani, D., LeCain, M. & Sheer, D. The role of microhomology in genomic structural variation. *Trends Genet.* **30,** 85–94 (2014).
43. Iraqui, I. *et al.* Recovery of arrested replication forks by homologous recombination is error-prone. *PLoS Genet.* **8,** e1002976 (2012).
44. Benson, E. K. *et al.* p53-dependent gene repression through p21 is mediated by recruitment of E2F4 repression complexes. *Oncogene* **33,** 3959–3969 (2014).
45. Bartkova, J. *et al.* Oncogene-induced senescence is part of the tumorigenesis barrier imposed by DNA damage checkpoints. *Nature* **444,** 633–637 (2006).
46. Liontos, M. *et al.* Modulation of the E2F1-driven cancer cell fate by the DNA damage response machinery and potential novel E2F1 targets in osteosarcomas. *Am. J. Pathol.* **175,** 376–391 (2009).
47. Gonzalez, S. *et al.* Oncogenic activity of Cdc6 through repression of the INK4/ARF locus. *Nature* **440,** 702–706 (2006).
48. Beauséjour, C. M. *et al.* Reversal of human cellular senescence: roles of the p53 and p16 pathways. *EMBO J.* **22,** 4212–4222 (2003).
49. Woo, R. A. & Poon, R. Y. Cyclin-dependent kinases and S phase control in mammalian cells. *Cell Cycle* **2,** 316–324 (2003).
50. Pines, J. & Hunter, T. Human cyclins A and B1 are differentially located in the cell and undergo cell cycle-dependent nuclear transport. *J. Cell Biol.* **115,** 1–17 (1991).
51. Yu, J. *et al.* A network of p73, p53 and Egr1 is required for efficient apoptosis in tumor cells. *Cell Death Differ.* **14,** 436–446 (2007).
52. Terradas, M., Martín, M., Tusell, L. & Genescà, A. DNA lesions sequestered in micronuclei induce a local defective-damage response. *DNA Repair (Amst)* **8,** 1225–1234 (2009).
53. Holland, A. J. & Cleveland, D. W. Chromoanagenesis and cancer: mechanisms and consequences of localized, complex chromosomal rearrangements. *Nat. Med.* **18,** 1630–1638 (2012).
54. Perkins, N. D. *et al.* Regulation of NF-κB by cyclin-dependent kinases associated with the p300 coactivator. *Science* **275,** 523–527 (1997).
55. Viale, A. *et al.* Cell-cycle restriction limits DNA damage and maintains self-renewal of leukaemia stem cells. *Nature* **457,** 51–56 (2009).
56. Shay, J. W. & Roninson, I. B. Hallmarks of senescence in carcinogenesis and cancer therapy. *Oncogene* **23,** 2919–2933 (2004).
57. Nishitani, H. *et al.* Two E3 ubiquitin ligases, SCF-Skp2 and DDB1-Cul4, target human Cdt1 for proteolysis. *EMBO J.* **25,** 1126–1136 (2006).
58. Niculescu, A. B. *et al.* Effects of p21(Cip1/Waf1) at both the G1/S and the G2/M cell cycle transitions: pRb is a critical determinant in blocking DNA replication and in preventing endoreduplication. *Mol. Cell. Biol.* **18,** 629–643 (1998).
59. Porter, A. C. Preventing DNA over-replication: a Cdk perspective. *Cell Div.* **3,** 3 (2008).
60. Hastings, P. J., Ira, G. & Lupski, J. R. A microhomology-mediated break-induced replication model for the origin of human copy number variation. *PLoS Genet.* **5,** e1000327 (2009).
61. Zhang, C. Z., Leibowitz, M. L. & Pellman, D. Chromothripsis and beyond: rapid genome evolution from complex chromosomal rearrangements. *Genes Dev.* **27,** 2513–2530 (2013).
62. Stephens, P. J. *et al.* Massive genomic rearrangement acquired in a single catastrophic event during cancer development. *Cell* **144,** 27–40 (2011).
63. Sikder, H. A., Devlin, M. K., Dunlap, S., Ryu, B. & Alani, R. M. Id proteins in cell growth and tumorigenesis. *Cancer Cell* **3,** 525–530 (2003).
64. Burrell, R. A., McGranahan, N., Bartek, J. & Swanton, C. The causes and consequences of genetic heterogeneity in cancer evolution. *Nature* **501,** 338–345 (2013).
65. Cha, H. H. *et al.* Glucocorticoids stimulate p21 gene expression by targeting multiple transcriptional elements within a steroid responsive region of the p21waf1/cip1 promoter in rat hepatoma cells. *J. Biol. Chem.* **273,** 1998–2007 (1998).
66. Georgakopoulou, E. A. *et al.* Specific lipofuscin staining as a novel biomarker to detect replicative and stress-induced senescence. A method applicable in cryo-preserved and archival tissues. *Aging* **5,** 37–50 (2013).

METHODS

Tumour specimens. Formalin-fixed, paraffin-embedded sections from 20 head–neck carcinomas, 30 urothelial bladder carcinomas, 30 lung carcinomas and 5 dysplasia-associated lesions or masses from patients with ulcerative colitis, which exhibit early p53 aberrations[17], were analysed and have been previously described[14,67]. Patients had not undergone any chemo-, immune- or radiotherapy. Protocols for clinical sample collection and their experimental use were approved by the Bio-Ethics Committee of Medical School of Athens, in accordance with the Declaration of Helsinki and local laws and regulations, following also written consent from the patients.

Cell lines and culture treatments. Cell lines were maintained in DMEM (Invitrogen) with 10% FCS (Invitrogen), 2 mM L-glutamine (Invitrogen), and 100 µg ml^{-1} penicillin and streptomycin (Invitrogen) at 37 °C and 5% CO$_2$.

p21 and p21$^{(mut)PCNA}$ were subcloned from pRc–CMV vectors into pLVXTRE3G, correspondingly. Inducible Li–Fraumeni p21 Tet-ON, Li–Fraumeni and Saos2 p21$^{(mut)PCNA}$ Tet-ON cells were generated by introducing the p21- and the p21$^{(mut)PCNA}$-carrying pLVXTRE3G vectors in MDAH041 (Li–Fraumeni) fibroblasts and Saos2, respectively[18]. Clones with clear p21 and p21$^{(mut)PCNA}$ expression were selected.

Tet-ON inducible cell lines were treated with 1 µg ml^{-1} doxycycline (Applichem) and HT1080 p21-9 cells with 100 µM IPTG (Ambion). Saos2 and MDA-MD-234 were treated with 5 ng ml^{-1} TGF-β, while MCF cells with 2 µM doxorubicin (Sigma).

Microphotographs were obtained with an inverted microscope (Axiovert S100; Carl Zeiss) equipped with CP-Achromat objectives and a CCD (charge-coupled device) IRIS colour video camera (SSC-C370P; Sony), using Image Pro Plus v3.0 (Media Cybernetics) software.

No cell lines used in this study were found in the database of commonly misidentified cell lines that is maintained by ICLAC and NCBI Biosample. All cell lines have been authenticated by STR profiling and are regularly tested to exclude mycoplasma contamination.

siRNA transfections and retrovirus infections. CDC6, CDT1, Rad52, Rad51, p21, FZR1 (Thermo Scientific) and Mus81, p73 (Santa Cruz) siRNA gene silencing was performed as described, following the manufacturer's instructions[46].

Saos2 cells were transiently infected with pMSCV, pMSCV–p21 or pMSCV–p21$^{(mut)PCNA}$ (a mutant p21 harbouring Gln144, Met147 and Phe150 substitutions to alanine in its PIP degron motif) vectors using the Phoenix helper-free retrovirus producer cell line as previously described[49].

Immunohistochemistry. Immunohistochemistry was performed as previously published using the UltraVision LP Detection System (no. TL-060-HD, Thermo Scientific) according to the manufacturer's instructions[67]. Primary antibodies are described in Supplementary Table 23. Evaluation and controls for Ki67 and p21 have been previously described[67].

Indirect immunofluorescence. Indirect immunofluorescence analysis was performed as previously published[14]. Primary antibodies are described in Supplementary Table 23. Secondary antibodies were Alexa Fluor 488 goat anti-rabbit (Invitrogen, no. A11034, 1:500) and Alexa Fluor 568 goat anti-mouse (Invitrogen, no. A110-31, 1:500). Image acquisition of multiple random fields was automated on a ScanR screening station (Olympus) and analysed with ScanR (Olympus) software, or a Zeiss Axiolab fluorescence microscope equipped with a Zeiss Axiocam MRm camera and Achroplan objectives, while image acquisition was performed with AxioVision software 4.7.1.

Electron microscopy analysis of DNA RIs in human cells. The procedure was performed as previously described[35]. Images were obtained with a transmission electron microscope (Tecnai G2 Spirit; FEI; LaB6 filament; high tension ≤120 kV) equipped with a side-mount CCD camera (2,600 × 4,000 pixels; Orius 1000; Gatan), processed with DigitalMicrograph Version 1.83.842 (Gatan) and analysed with ImageJ (National Institutes of Health).

Protein extraction, cell fractionation and immunoblotting. Protein extraction and cell fractionation (Supplementary Fig. 1di) was performed as described before[12,14]. Primary antibodies are described in Supplementary Table 23. Thirty micrograms of protein from total extracts or 1 µg of histones per sample was adjusted with Laemmli buffer (Sigma) and loaded on acrylamide/bis-acrylamide gels. Gel electrophoresis, transfer to PVDF membrane (Millipore) and signal development with nitro blue tetrazolium/5-bromo-4-chloro-3-indolylphosphate (NBT/BCIP) solution (Molecular Probes) or chemiluminescence were performed as previously described[12]. Alkaline phosphatase-conjugated anti-mouse or anti-rabbit secondary antibody (1:5,000 dilution) (Promega) was used.

In vivo ubiquitin assay. Saos2 p21 cells were treated with MG-132 proteasome inhibitor (MERCK) for 3 h at 30 µM at the time points indicated (Fig. 2d). Cells were lysed in RIPA buffer (50 mM Tris-HCl pH 8.0, 150 mM NaCl, 0.1% SDS, 1% sodium deoxycholate, 1% Triton X-100, protease inhibitor cocktail (Thermo Scientific), phosphatase inhibitor cocktail (Thermo Scientific), N-ethylameleimide deubiquitylase inhibitor (Applichem)). Protein lysates were precleared with protein G agarose beads (Millipore) for 1 h and then incubated with G-protein beads bound to CDT1 antibody (Supplementary Table 23) for 2 h at 4 °C. Beads were washed three times in RIPA buffer containing protease, phosphatase and deubiquitylase inhibitors, as above. Protein was eluted from beads with 2× SDS–β-mercaptoethanol sample buffer, boiled for 8 min and loaded on polyacrylamide gels for SDS–PAGE as described above. Blots were blocked for 1 h in 5% BSA in TBS-0.1% (v/v) Tween-20 solution at room temperature. Membranes were incubated overnight with CDT1 antibody (Supplementary Table 23) in 5% BSA in TBS supplemented with 0.1% (v/v) Tween-20, followed by a 1 h incubation with HRP- conjugated anti-mouse secondary antibody (R&D Systems) at 1:1,000 dilution at room temperature. Signal development was performed with NBT/BCIP solution (Molecular Probes) according to the manufacturer's instructions.

CDK2 kinase activity. For each sample, 50 mg of total-cell protein extract was precleared for 2 h at 4 °C with 5 mg of rabbit immunoglobulin G (anti-Cdk2) or 5 mg of mouse immunoglobulin G (anti-cyclin B1) prebound to protein A–Sepharose (Upstate-Millipore). Precleared lysates were collected and incubated with anti-Cdk2, or anti-cyclin B1 with mixing for 2 h at 4 °C. Protein A–Sepharose was added, and the samples were mixed for 2 h at 4 °C. The immunoprecipitates were washed twice with TBS and twice with kinase buffer (100 mM Tris (pH 7.4), 20 mM MgCl$_2$, 2 mM dithiothreitol) and incubated with 5 mg of histone H1 (Boehringer), 15 nM ATP for 10 min at 25 °C. Samples were incubated with malachite green reagent for 30 min (Cdk2 and cyclin B1). Kinase assay mixtures were quantified at 620 nm by subtracting negative control.

Chromatin immunoprecipitation (ChIP) assay. ChIP assay was performed as previously described[12]. A 100 bp fragment in the *Rad51* promoter and a 110 bp amplicon, located approximately 1,000 bp from the transcription start site (Fig. 5l), were amplified. Primers and annealing temperatures are provided in Supplementary Table 24. PCR reactions containing 1% of the total chromatin extract used in the immunoprecipitation reactions were used as inputs.

Comet assay. The comet assay was performed as previously described[12]. Cells were observed under a Zeiss Axiolab fluorescence microscope equipped with a monochrome CCD camera. Analysis was conducted with Cometscore software (Tritek). All experiments were performed in triplicates.

Pulsed-field gel electrophoresis. This technique has been previously described[31].

DNA fibre spreadings. This technique was conducted as previously described with slight modifications[45]. Briefly, Saos2 p21 cells were grown in the presence or absence of doxycycline for 4 days and then pulsed-labelled with 25 µM CldU for 20 min, and then labelled with 250 µM IdU for 20 min. Cells were then harvested and lysed on glass slides in spreading buffer. The DNA was denatured and stained with rat anti-BrdU/CldU (1:1,000, OBT0030F, Immunologicals Direct) and mouse anti-IdU/BrdU (1:500, clone B44, Becton Dickinson) primary antibodies.

Isolation of nucleic acids and bisulfate treatment. DNA extraction was performed as previously described[14]. RNA was extracted with the RNeasy Mini Kit (no. 74104, Qiagen). For assessing DNA methylation levels of p73 promoter, 1 µg DNA was bisulfite-converted using the EZ-DNA Methylation Gold kit (ZymoResearch) as per the supplier's guidelines and eluted in 30 µl of elution buffer.

cDNA preparation and real-time quantitative PCR with reverse transcription (RT–rt-qPCR). cDNA generation and RT–rt-qPCR analysis was run as described before[67]. DNA methylation levels for p73 promoter were assessed by high-resolution-melting (HRM) analysis. The reaction was performed in a StepOne Real time machine (Life Technologies) using Universal Master Mix II without UNG containing SYBR (Life Technologies) and 200 nM primers. A dissociation (melt) curve programme followed at the end of 40 cycles. Signal analysis was carried out using the StepOne v2.3 software. SssI-methylated and -unmethylated DNA was run in parallel as positive and negative controls, respectively. Primer sequences and annealing temperatures are provided in Supplementary Table 24. Results are presented as *n*-fold changes for the various time points after p21 induction versus the values of the non-induced sample. Mean value was calculated from three independent measurements.

Flow cytometric analysis (FACS). Cell-cycle analysis was assessed on a FACS Calibur (Becton Dickinson) as described before[14].

For BrdU pulse-chase proliferation assays, cells were pulse-labelled with 10 μM BrdU (Roche) for 1 h, fixed in 70% ethanol, and incubated in 2 M HCl for 30 min. Cells were incubated with mouse antibody against BrdU (1:100) for 1 h. For EdU analysis, cells were either pulsed for 10 min or 24 h with 10 μM EdU. Cells were fixed in 70% ethanol and incubated with mouse anti-γ-H2AX or mouse anti-p21 for 30 min (see Supplementary Table 23), followed by a further 15 min incubation with Alexa Fluor 488 anti-mouse IgG (1:100, no. A-11029, Invitrogen) or anti-mouse E-Phycoerythrin (1:100, Invitrogen). EdU was detected with a Click-iT EdU Cell Proliferation Assay kit (Invitrogen-C10420).

For MCM2 staining, cells were washed once in wash buffer (1% (w/v) BSA in PBS), while unbound MCM2-7 was extracted in freshly prepared CSK buffer (10 mM HEPES, 100 mM NaCl, 3 mM $MgCl_2$, 1 mM EGTA, 300 mM sucrose, 1% (w/v) BSA, 0.2% (w/v) Triton-X100, 1 mM dithiothreitol, 1 mM phenylmethyl sulfonyl fluoride, 10 ng ml^{-1} pepstatin, 10 ng ml^{-1} leupeptin and 10 ng ml^{-1} aprotinin) on ice for 10 min. Extracted cells were then fixed in 2% (v/v) paraformaldehyde in PBS for 10 min at 37 °C, washed twice in wash buffer and stored in wash buffer at 4 °C until staining. CSK-extracted fixed cells were permeabilized in ice-cold 70% (v/v) ethanol for 10 min at room temperature, washed in wash buffer and incubated for 1 h at room temperature with mouse monoclonal anti-human MCM2 (BM28 no. 610700, BD Biosciences) diluted 1:500 in wash buffer. Cells were then washed once in wash buffer and incubated for 30 min at room temperature in the dark with Alexa Fluor 488 goat anti-mouse secondary antibody (no. A-11029, Invitrogen) diluted 1:500 in wash buffer, before being washed twice in wash buffer and resuspended in 50 μg ml^{-1} 7-AAD (7-aminoactinomycin D, Life Technologies) diluted in wash buffer. Samples were analysed using FACS Canto (Becton Dickinson) and the BD FACS DIVA software (BD Biosciences). Data analysis was performed using Flowjo (version 7.6.5, Tree Star Inc.). To quantify G1 MCM levels, the Flowjo software was used to gate on cells with a G1 DNA content and then the mean, median, and 95th and 99th percentiles of the Alexa Fluor 488 levels in the G1 cells were calculated for each replicate; the data are presented with the background mean, median, 95th percentile or 99th percentile subtracted to correct for the increase in auto-fluorescence.

Senescence staining. Control (OFF) and induced (ON) Saos2 p21 Tet-ON or MDAH041 p21 Tet-ON cells were fixed in 1% paraformaldehyde and then processed for SA-β-gal or Sudan Black B staining and counterstained with nuclear fast red, as described elsewhere[66]. Only cytoplasmic staining was scored as positive signal.

MTT assay. Cytotoxicity was estimated by the MTT (3-[4,5-dimethylthiazol-2-yl]-2,5-diphenyltetrazolium bromide) assay[12]. Data from three independent measurements were averaged and the corresponding s.d. is also reported.

Soft agar and invasion assays. Soft agar and invasion assays were performed as described elsewhere[12]. Experiments were performed in three independent replicates.

***In vitro* tumour sphere formation assays.** Saos2 Tet-On p21 (10⁴) cells were suspended in sphere formation medium (serum-free DMEM/F12 medium (Invitrogen) supplemented with 20 ng ml^{-1} epidermal growth factor (EGF, Sigma), 20 ng ml^{-1} basic fibroblast growth factor (bFGF, Sigma) and 1× B27 supplement (Invitrogen)) in ultralow-attachment 6-well plates (Corning). Cells were cultured under 5% CO_2 at 37 °C for 15 days. The number of generated spheres were counted and sized under an inverted microscope (Axiovert S100; Carl Zeiss) equipped with CP-Achromat objectives. Subsequently, medium with spheres was aspirated, treated with trypsin to dissociate cells from spheres and centrifuged (Fig. 8k). Cell pellets were resuspended in fresh medium, counted and plated on soft agar, as previously described[12]. Data from three independent measurements from this combined procedure were averaged and the corresponding s.d. is reported.

Molecular cytogenetics. Molecular cytogenetics analyses were conducted as previously reported[12]. Cytogenetic analyses were performed using a 63× magnification lens on a fluorescent Axio-Imager Z1, Zeiss microscope, equipped with a MetaSystems CCD camera and the MetaSystems Isis software.

High-throughput analyses. *Proteomics.* Total protein was extracted from two biological replicates of non-induced and 12-h-, 48-h- and 96-h- induced Saos2-p21 Tet-ON cells (n = 2 experiments), where protein digestion and 8plex-iTRAQ labelling was performed as previously described[16]. The pooled whole sample was split in two equal parts lyophilized and stored at −20 °C. To the first half of the aforementioned iTRAQ-labelled sample high-pH reverse-phase peptide fractionation was performed as previously described[16]. The second half

of the iTRAQ-labelled peptides was fractionated with hydrophilic interaction chromatography as previously described[68].

The individual high-pH reverse-phase and HILIC peptide fractions were analysed by LC–MS/MS followed by database searching as previously described[69].

High-throughput whole-genome analyses. aCGH analysis. Genomic DNA from 30 days induced and non-induced Saos2- and Li–Fraumeni-p21 Tet-ON cells was extracted using the BioRobot M48 System (Qiagen) and the MagAttract DNA Blood Midi M48 Kit (Qiagen). Quality and quantity of the DNA samples was determined on a NanoDrop ND-1000 UV–VIS spectrophotometer.

Agilent Human Genome CGH 4 × 180 K (to analyse Saos2-p21 escaped and non-induced, each comprising two biological replicates) and 1 × 1 MK (to analyse Saos2-p21 escaped and non-induced, each comprising two biological replicates; and Li–Fraumeni-p21 escaped and non-induced, each comprising three biological replicates, (n = 3)) microarrays were used. Labelling and hybridization was carried out according to the manufacturer's guidelines. Data were processed using Feature Extraction 10.7.3.1 and analysed using Cytogenomics 2.7.22.0 software (Agilent) with the following settings: Algorithm: ADM-1, Threshold: 6.7, with a minimum of four probes for a region to be included. Centralization and fuzzy zero corrections were applied to remove putative variant intervals with small average log$_2$ ratios as compared to the noise level that was determined by the system.

Whole-genome sequencing (WGS). Genomic DNA from two biological replicates obtained at 30 days' induction and non-induction of Saos2- and Li–Fraumeni-p21 Tet-ON cells, respectively, was used for WGS. The library preparation and the WGS were carried out in the Greek Genome Center (GGC) of Biomedical Research Foundation of Academy of Athens (BRFAA) and in EMBL Genecore facility.

WGS was performed achieving 20–30× coverage of the human genome with paired-end sequencing (2 × 150 and 2 × 100 bp). Quality control was performed with fastqc software[70] and alignment to the human genome (GRCh37/hg19 version) was performed with the bowtie2 algorithm[71]. Samtools[72] was used to convert sam files to bam and for sorting bam files. Breakdancer software[73] (breakdancer-1.1-2011_02_21 version) was utilized to identify SV (intra- and inter-chromosomal translocations, deletions, insertions and inversions).

Use of breakdancer with default parameters led to identification of new inter-chromosomal translocations in 'ON' versus 'OFF' cells in both cell types (Supplementary Fig. 7). To identify microhomology regions in the inter-chromosomal translocations observed in both systems we used the coordinates from the breakdancer output and extended 30 bp on both sides of the breakpoint junction. Clustal W was used for aligning the regions around the breakpoint junctions. Microhomology regions identified on the breakpoint spanned from 2–38 bp.

RNA-seq analysis. RNA was collected from non-induced, 10 days (10 d) and 'escaped' Li–Fraumeni p21 Tet-ON cells (six biological replicates for escaped (n = 6) and four biological replicates for non-induced (n = 4)). RNA-seq library preparation and analysis procedure was performed as described before[8].

Expression microarray analysis. Total RNA was isolated from three biological replicates of non-induced and 12-h-, 48-h- and 96-h-induced Saos2-p21 Tet-ON cells (n = 3), using the RNeasy Total RNA kit (Qiagen) following the manufacturer's instructions. Microarray analysis was performed by the microarray unit of CBM Core Facility Italy (http://www.cbm.fvg.it) using Illumina's Whole-Genome Expression Beadchip. Integrity of total RNA was evaluated using capillary electrophoresis (Bioanalyzer 2100, Agilent) and quantified using a Nanodrop 1000. Aliquots of RNA (250 ng) samples were amplified according to specifications of the Illumina TotalPrep RNA Amplification Kit (Ambion) to produce a pool of biotin-labelled RNA corresponding to the polyadenylated (mRNA) fraction. The cRNA samples were applied to whole-genome HumanHT-12 v4.0 arrays (Illumina) and hybridized according to the manufacturer's specification. The signal intensities from the hybridization images were extracted and background subtracted using Illumina BeadStudio (v3.3.7). Data were checked for the Illumina internal quality control.

Total RNA was extracted from the non-induced and 'escaped' Saos2-p21 Tet-ON cells using Trizol (Life Technologies) and chloroform/isoamyl alcohol (49:1) (four biological replicates for escaped (n = 4) and three biological replicates for non-induced (n = 3)). Targets were prepared using the GeneChip Whole Transcriptome (WT) Plus reagent kit and hybridized to Affymetrix GeneChip Human Transcriptome array 2.0 (HTA 2.0). The obtained Saos2-p21 transcriptome profile was compared with the Li–Fraumeni p21 transcriptome profile obtained by RNA-seq.

Bioinformatic analysis. *Transcriptome and proteome analyses from non-induced, 12-h-, 48-h- and 96-h-induced Saos2-p21 Tet-ON cells.* Protein and gene ratios (time point/time 0) were log$_2$ transformed and centred. Statistically significant differentially expressed genes and proteins ($P < 0.05$) were determined by normal distributions of the log$_2$ ratios and ANOVA plus Kruskal–Wallis (Kruskal–Wallis only for the transcriptome data set where n = 3) since there was more than one

time point. For the proteomic data set that consisted of two biological replicates, ANOVA was used on the basis of the conclusion of previous reports[74] that there are no principal objections to using t-tests and ANOVA with sample replicates as small as 2. All calculations were performed with R. The 'Gene-Set Enrichment Analysis' on the Gene Ontology biological process set was performed as previously described[16]. Pathway visualization for all data sets was performed with Ariadne Genomics Pathway Studio v9.0.

Transcriptome analysis from non-induced and 'escaped' Saos2-p21 Tet-ON cells. Affymetrix .CEL files were normalized with the Robust Multi-array Average (RMA) algorithm. Data were further analysed by principal component analysis and one-way ANOVA ($P < 0.05$). Differentially expressed transcripts were analysed using the Ingenuity Pathway Analysis software considering all direct and indirect relationships obtained only from experimentally verified information.

WGS and aCGH data comparison. To compare the WGS data with the aCGH data regarding DNA copy-number aberrations in 'escaped' (ON) cells versus control (OFF) cells (both in Saos2 and Li–Fraumeni systems), the WGS data were processed as follows: genomic regions presenting less than 10-times coverage were filtered out to ensure data high quality; the $\log_2$ of the ratio of the normalized reads in the 'escaped' cells over the normalized number of reads in the control cells was calculated; for each chromosome the aforementioned $\log_2$ ratios underwent DNA copy-number segmentation analysis using the circular binary segmentation algorithm through the Bioconductor package 'DNAcopy'[75].

Assessment of randomness in the overlap between the transcriptomics and aCGH data through Monte Carlo simulation. To access the probability of the observed overlap between the transcriptionally affected genes (DNA-microarray for Saos2 and RNA-Seq for Li–Fraumeni p21 Tet-ON systems) and the genes present in the significantly affected genomic regions (aCGH data) being due to chance, a Monte Carlo simulation approach was utilized. Specifically, the genes present on the corresponding transcriptomics analysis platform (DNA-microarray for Saos2 and RNA-Seq for Li–Fraumeni) were randomly sampled 10^4 times with a sample size equal to the number of significantly regulated genes. For each random sampling the overlap with the genes present in regions exhibiting genomic aberrations according to aCGH was calculated. The distribution of the number of overlaps was found to be normal according to the Kolmogorov–Smirnov test for normality; hence, the P value of the observed overlap in our data was calculated. That P value represents the probability of the observed overlap to belong to the distribution of the randomly generated overlaps, therefore being due to chance alone. All statistical analysis was carried out with R. *Pathway Analysis.* Proteomics and transcriptomics data were analysed with Ariadne Pathway Studio v9.0 as previously described[16].

Statistics and reproducibility. Parametric (two-sided t-test and one-way ANOVA) and non-parametric tests (Mann–Whitney and Kolmogorov–Smirnov test for normality), were used for hypothesis testing with P values < 0.05 considered as significant.

Immunoblots presented in Figs 1e, 3a,b,d,e, 4a,c and 6d–g are representative of three different experiments. Photos of Figs 1d, 5a–d and 7a,b are representative of at least two independent experiments.

67. Evangelou, K. *et al.* The DNA damage checkpoint precedes activation of ARF in response to escalating oncogenic stress during tumorigenesis. *Cell Death Differ.* **20,** 1485–1497 (2013).
68. Delehouzé, C. *et al.* CDK/CK1 inhibitors roscovitine and CR8 downregulate amplified MYCN in neuroblastoma cells. *Oncogene* **33,** 5675–5687 (2014).
69. Papachristou, E. K. *et al.* The shotgun proteomic study of the human ThinPrep cervical smear using iTRAQ mass-tagging and 2D LC-FT-Orbitrap-MS: the detection of the human papillomavirus at the protein level. *J. Proteome Res.* **12,** 2078–2089 (2013).
70. Ramirez-Gonzalez, R. H. *et al.* StatsDB: platform-agnostic storage and understanding of next generation sequencing run metrics. *F1000Res.* **2,** 248 (2013).
71. Langmead, B. & Salzberg, S. L. Fast gapped-read alignment with Bowtie 2. *Nat. Methods* **9,** 357–359 (2012).
72. Li, H. *et al.* 1000 genome project data processing subgroup. The sequence alignment/map format and SAMtools. *Bioinformatics* **25,** 2078–2079 (2009).
73. Chen, K. *et al.* BreakDancer: an algorithm for high-resolution mapping of genomic structural variation. *Nat. Methods* **6,** 677–681 (2009).
74. de Winter, J. C. F. Using the Student's t-test with extremely small sample sizes. *Pract. Assess. Res. Eval.* **18,** 10 (2013).
75. Venkatraman, E. S. & Olshen, A. B. A faster circular binary segmentation algorithm for the analysis of array CGH data. *Bioinformatics* **23,** 657–663 (2007).
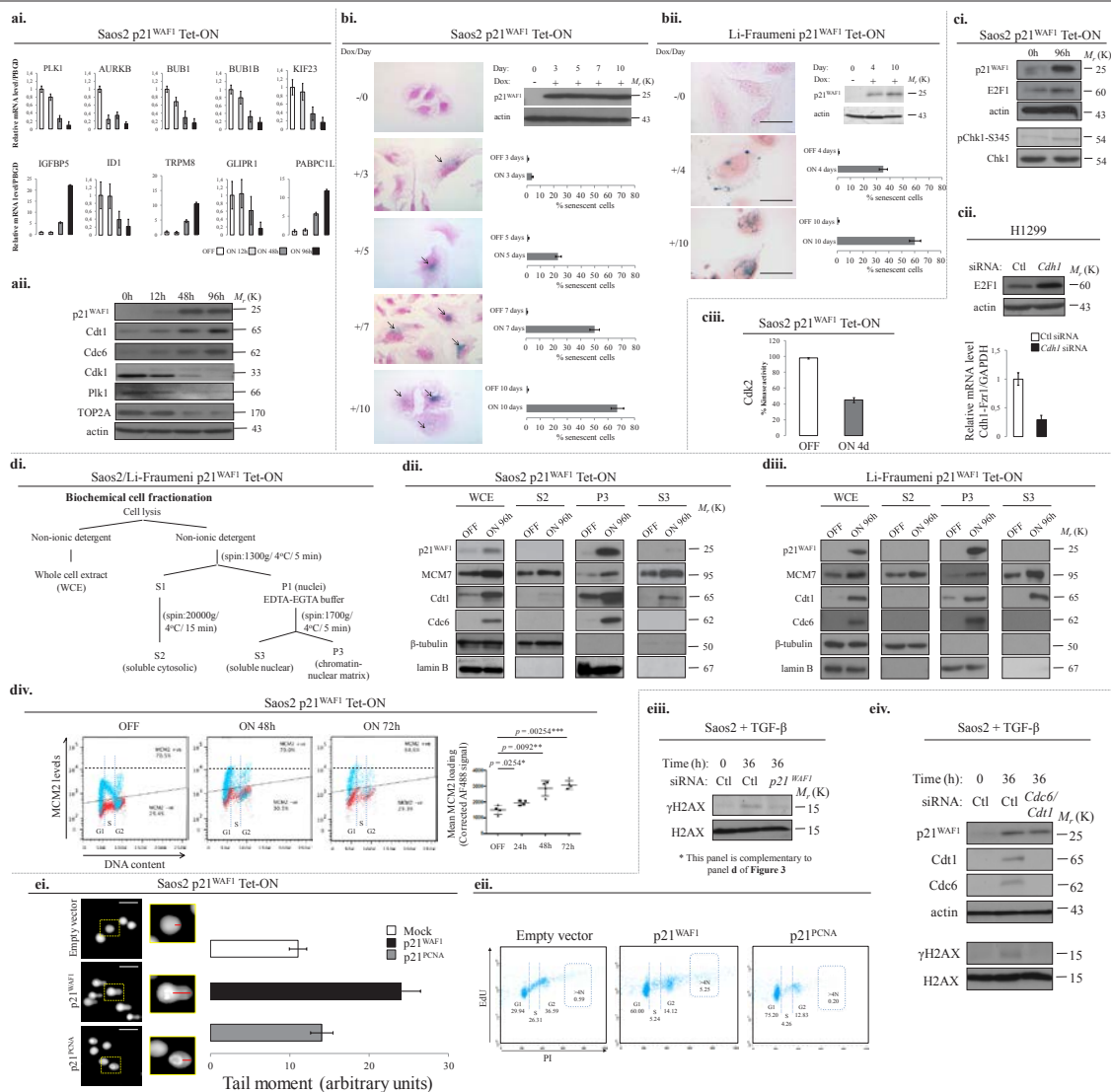
Supplementary Figure 1 (a) Representative factors affected by p21WAF1/Cip1 induction at transcriptional and translational level. Representative real-time RT-PCR analyses to validate the high-throughput expression results (see also **Fig. 2**) ($p < 0.01$, t-test, error bars indicate mean +/- SDs, n=3 experiments). **i.** Mitotic factors: PLK1, AURKB, BUB1, BUB1B, KIF23 and the pro-apoptotic factor GLIPR1 along with the suppressor of the p21WAF1/Cip1 mediated effects ID1 are transcriptionally downregulated at the indicated time points in Saos2 p21WAF1/Cip1 Tet-ON induced cells. Growth factor IGFBP5, the ion channel encoding gene TRPM8 and the poly-A binding protein PABPC1L are upregulated. PBGD: Porphobilinogen deaminase (house-keeping gene) **ii.** Representative immunoblots that validate the proteome. Actin serves as a loading control. (PLK1: Polo-like kinase-1; AURKB: Aurora kinase B; BUB1: budding uninhibited by benzimidazoles 1 homolog; KIF23: kinesin family member 23; GLIPR1: Glioma pathogenesis related 1; ID1: inhibitor of DNA binding 1; IGFBP5: insulin-like growth factor binding protein 5; TRPM8: transient receptor potential cation channel subfamily M member 8; PABPC1L: poly(A) binding protein, cytoplasmic 1-like; TOP2A: topoisomerase 2A). **(b)** Timeline of senescence appearance in Saos2 p21WAF1/Cip1 Tet-ON and Li-Fraumeni p21WAF1/Cip1 Tet-ON induced cells. Activation of the senescence barrier occurs at approximately day 3 of induction in both cellular systems and increases gradually, reaching its highest value at around day 10, while no signs of senescence are evident in untreated cells grown for the same time period (as corresponding graphs depict). p21WAF1/Cip1 was confirmed by western blot (upper right panel). **(c) i.** E2F1 is upregulated while Chk1 is activated upon prolonged p21WAF1/Cip1 induction. Lysates from Saos2 p21WAF1/Cip1 Tet-ON cells, after treatment with 1µg /ml Doxycycline for the depicted time points, were separated by SDS-PAGE and immunoblotted to detect the indicated proteins. **ii.** Silencing of Cdh-1/FZR-1 leads to increase in E2F1 expression in the p53 null H1299 cells. **iii.** A decline of Cdk2 activity is observed following p21WAF1/Cip1 induction. Histogram depicting decreased Cdk2 activity at days 4 after p21WAF1/Cip1 induction. **(d)** MCM2-7 chromatin loading is increased following p21WAF1/Cip1 induction in Saos2 and Li-Fraumeni cells. **i.** Diagram describing cell fractionation experimental algorithm. **ii-iii.** All fractions were separated by SDS-PAGE and were analyzed by IB in Saos2 cells (ii) and Li-Fraumeni cells (iii). Lamin-B serves as fractionation control, while β-tubulin as loading control (n=3 experiments). **iv.** FACS analysis of MCM2 chromatin loading in induced Saos2 p21WAF1/Cip1 Tet-ON cells versus non-induced (red dots, -ve: control experiment with no MCM2 antibody; blue dots, +ve: experiment with MCM2 antibody) (* $p < 0.05$, ** $p < 0.01$, *** $p < 0.005$, t-test, error bars indicate mean +/- SDs, n=3 experiments). **(e)** Re-replication and DNA damage was significantly lesser in Saos2 cells infected with p21PCNA mutant. **i.** Comet assays showed DNA breaks in cells infected with the indicated constructs (see also **Fig. 4b,d,f**) ($p < 0.0001$, *ANOVA*, error bars indicate mean +/-SDs, n=3 experiments). Red lines in magnifications of insets label comet (moment) tails for length comparison. **ii.** FACS analysis of the corresponding treatments. **iii.** DNA damage is p21WAF1/Cip1 dependent in Saos2 cells treated with TGF-β (n=3 experiments). **iv.** p21WAF1/Cip1 dependent DNA damage, in Saos2 cells treated with TGF-β, is exerted via Cdc6/Cdt1 mediated replication stress. (Empty vector: pMSCV, p21PCNA: mutant p21WAF1/Cip1 harboring Q144, M147, F150 substitutions to A in its PIP degron motif). Source data can be found in Supplementary Table 25.

Supplementary Figure 2. (a) Silencing of p21$^{WAF1/Cip1}$ in induced (ii.) Saos2- and (iii.) Li Fraumeni- p21$^{WAF1/Cip1}$ Tet-ON cells alleviates replication stress, DNA damage, senescence induction and enhanced resistance to chemotherapeutic drugs. Timeline of the experimental procedure is also depicted (i.). cells (p = NS, t-test or *ANOVA*, error bars indicate mean +/- SDs, n=3 experiments) Bars: 20μm (IF), 30μm (comet). **(b)** PCNA staining patterns reveal that sustained p21$^{WAF1/Cip1}$ expression, in cells with non-functional p53, "traps" cells mainly in early S-phase. IF analysis for assessing PCNA staining patterns in non-induced and 96h induced cells. Histograms depict average of observed patterns in the induction conditions employed (mean +/- SDs, n=3 experiments). Scale bars: 10 μm. **(c)** Absence of nascent ssDNA in Saos2 p21$^{WAF1/Cip1}$ Tet-ON expressing cells. p21$^{WAF1/Cip1}$ expression was induced for 96h with 1μg/ml doxycycline. The newly synthesized DNA was labeled for 20 min with 10 μM BrdU. 2 mM HU and 5 μM ATRi were added after the BrdU pulse as indicated for 2 h. After the indicated treatments, cells were fixed and stained with antibodies against BrdU without DNA denaturation to selectively detect nascent-strand ssDNA. Bars: 40μm. **(d)** P21$^{WAF1/Cip1}$ mediated DNA damage is processed by MUS81 resolvase. **i.** IF staining of DDR markers (53BP1 and γH2AX) in Saos2 p21^{WAF1} Tet-ON induced cells for 96h, with or without anti-*MUS81* siRNA targeting. Histogram depicts quantification of 53BP1 and γH2AX foci/cell (p < 0.01, t-test, error bars indicate mean +/- SDs, n=3 experiments). Bars: 20μm. **ii.** DNA damage assessed by comet assay after prolonged expression in Li-Fraumeni p21^{WAF1} Tet-ON cells (p < 0.01, t-test, error bars indicate mean +/- SDs, n=3 experiments). Bars: 50μm. **iii.** Silencing of the homologous repair recombinase *Rad51* resulted in decreased γH2AX levels in Li-Fraumeni p21^{WAF1} Tet-ON cells (p < 0.0001, *ANOVA*, error bars indicate mean +/- SDs, n=3 experiments). **(e)** Sustained expression of p21$^{WAF1/Cip1}$ in cells with non-functional p53 leads to restoration of Cdk2 activity in "escaped" cells. **i.** Following an initial decline (days 2-12) Cdk2 activity is increased in "escaped" cells (after day 20) (p < 0.01, t-test, error bars indicate mean +/- SDs, n=3 experiments). **ii.** Expression levels of p21$^{WAF1/Cip1}$ in the "escaped" (i) Saos2 and (ii) Li-Fraumeni p21^{WAF1} Tet-ON cells were similar or even higher sometimes (see **Fig. 7g**) to those observed in the initial phase of p21$^{WAF1/Cip1}$ induction. **(f)** Potential mechanisms involved in p73 down regulation in the "escaped" Saos2- and Li-Fraumeni-p21 cells. (see Fig 7g) **i.** Absence of p73 promoter methylation and genetic loss at *TP73* locus (1p36.33) (see Supplementary Fig. S5, S6; Supplementary Table 4). Representative result from real-time PCR followed by high resolution melting (HRM) analysis is depicted (n=3 experiments). Ctl DNA: SssI methylated and unmethylated control DNA. **ii.** Bioinformatic analysis employing Ingenuity software revealed potential factors that regulate p73 expression and activity. EGR-1 (Early Growth Response-1) is a potent transcriptional up-regulator of p73.[51] In turn, p73 can also transcriptionally induce EGR-1exprresion, forming a positive feed-back loop. HECW2 (HECT, C2 αnd WW Domain Containing E3 Ubiquitin Protein Ligase 2) expression stabilizes p73 protein levels via mono-ubiquitination,[1] while PRKACB (Protein Kinase A Catalytic Subunit β) decreases p73 transactivation and intramolecular interaction capacity.[2] **iii.** *TP73* gene locus organization and structure of p73 protein with HECW2 and PRKACB interacting domains. Yellow rectangles: transcribed non translated *TP73* exons; Blue rectangles: transcribed *TP73* exons; Green rectangle: P1 promoter of *TP73* gene; Blue ovals: EGR-1 biding sites. TDA: transactivation domain; DBD: DNA binding domain; OD: oligomerization domain; SAM: sterile alpha-motif domain. **iv-v.** Analysis of EGR-1, HECW2 and PRKACB expression status in "escaped" Saos2 p21$^{WAF1/Cip1}$ cells at mRNA (iv.) and protein (v.) level validated results obtained from high-throughput transcriptome analysis (Supplementary Fig. S3). CREB phosphorylation was examined as a proof-of-concept for PRKACB activity. **vi.** Analysis of EGR-1 at mRNA and protein level in "escaped" Li-Fraumeni p21$^{WAF1/Cip1}$ cells (fold difference mean +/- SDs, n=3 experiments). **vii.** Potential mechanism for p73 downregulation in "escaped" cells. Decreased levels of EGR-1 possibly represent the main reason for low p73 expression.[49] Additionally, high levels of PRKACB decreases p73 transactivation and intramolecular interaction abilities,[2] countering the ability of high HECW2 expression to stabilize p73 via mono-ubiquitination.[1] High PRKACB levels may contribute further to p73 down-regulation by interfering with the positive feed-back loop between ERG-1 and p73.[2] **(g)** Serial-section immunohistochemical (IHC) analysis showed co-expression of p21$^{WAF1/Cip1}$, Ki67 and Cdc6/Cdt1 in atypical cancer cells in head and neck carcinomas, urothelial carcinomas and precancerous lesions. Actin serves as a loading control. Source data can be found in Supplementary Table 25.
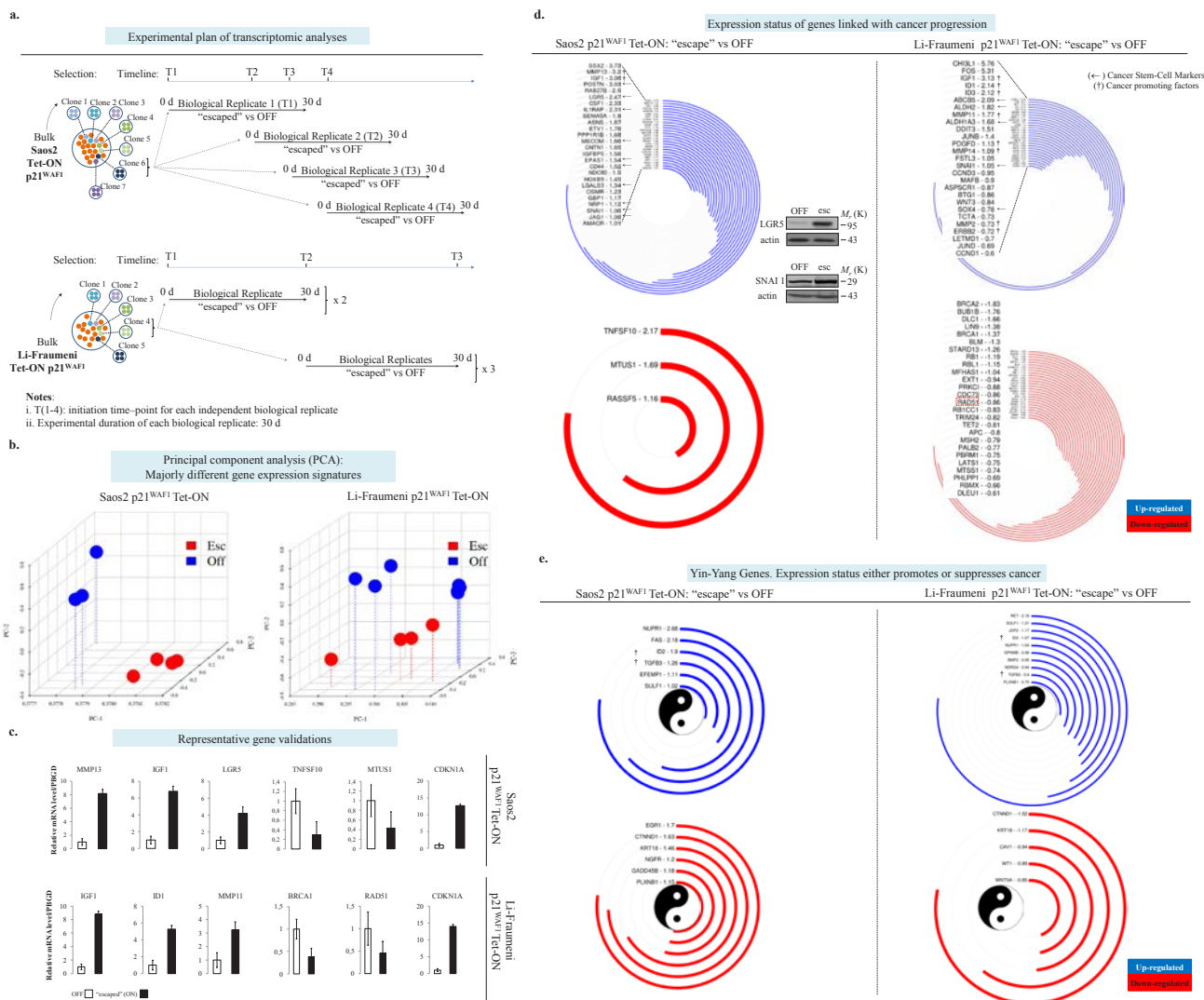
Supplementary Figure 3 Differentially expressed genes whose expression status affects cancer according to literature in Saos2- and Li-Fraumeni-p21 cells. Expression status of genes associated with cancer progression (see also Supplemental Table 8). **(a)** Timeline of experimental planning of transcriptome analyses. **(b)** Principal Component Analysis (PCA) of the differentially expressed genes depicting the majorly different gene expression signatures over the (19540 in Saos2- and 25376 in Li-Fraumeni cells) transcripts analysed. **(c)** Validation of representative factors in "escaped" (ON) cells versus non-induced (OFF) Saos2 and Li-Fraumeni cells. Representative real-time RT-PCR analyses, validating the high-throughput expression analysis ($p < 0.01$, t-test, error bars indicate mean +/- SDs, n=3 experiments). **(d)** Relative expression levels given as log-2-ratios of differentially expressed genes ($p < 0.05$) of the "escaped" vs OFF-cells, whose expression status (up or down-regulated) is reported to promote carcinogenesis. Arrow (←) denotes genes conferring cancer stemness (see also Supplemental Tables 8Aa, 8Ba). Lysates from non-induced and escaped Saos2 p21$^{WAF1/Cip1}$ Tet-ON cells were immunoblotted to verify representatively the expression of the LGR5 cancer related stemness gene. **(e)** Differentially expressed genes whose expression status either promotes or suppresses cancer according to literature. Relative expression levels given as log-2-ratios of differentially expressed genes ($p < 0.05$) of the "escaped" vs OFF-cells. The lengths of the "encircled" lines depict the intensity of expression. Uncropped images of blots are shown in Supplementary Fig. S9. Source data can be found in Supplementary Table 25.

Saos2 Tet-ON p21^WAF1
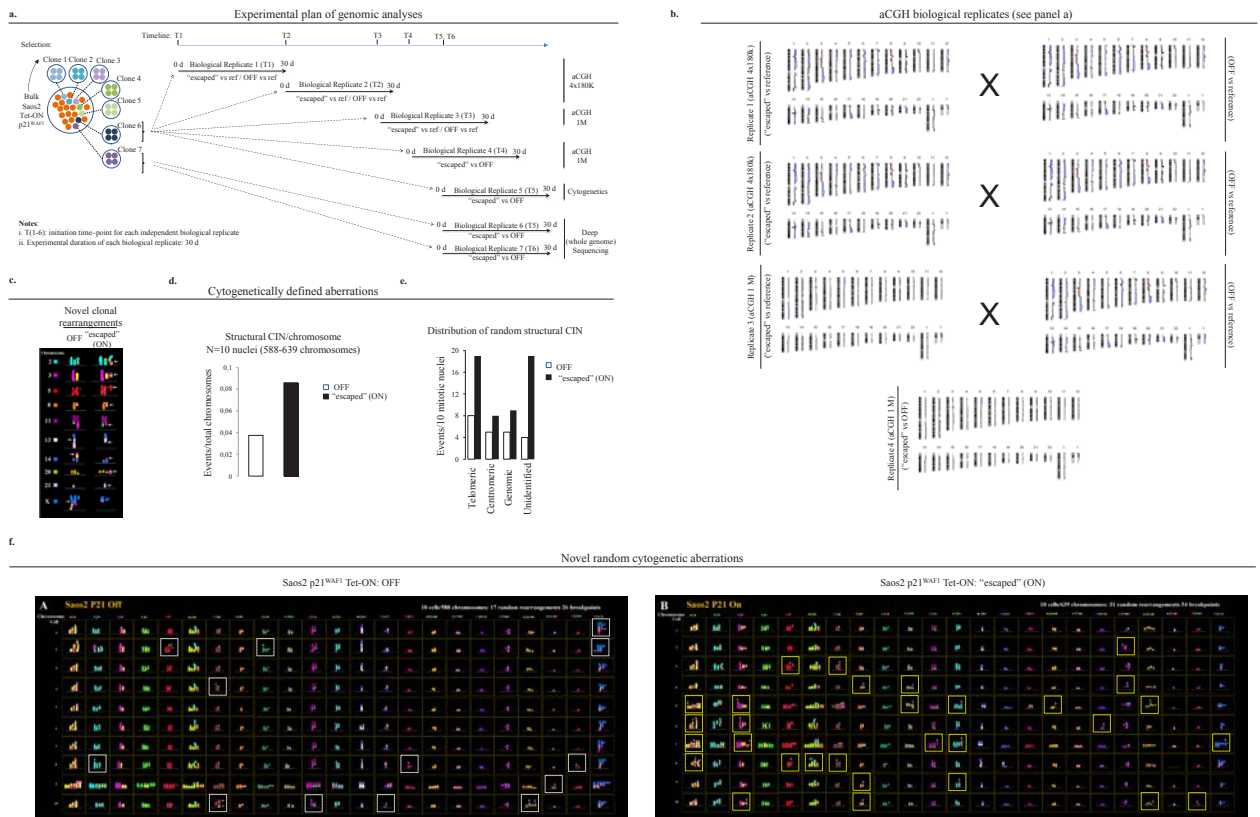
Supplementary Figure 4 "Escaped" Saos2 p21^WAF1/Cip1 cells exhibit increased genomic instability relative to non-induced cells. **(a)** Timeline of experimental planning of genomic analyses. **(b)** Overview of all array-CGH (aCGH) analyses results. In total 41 aberrations were found involving all chromosomes (except 9, 12, 14 and 15). The aberrations included 19 gains and 22 losses (Supplemental Table 5). The majority of aberrations were concentrated in chromosomes 3, 10 and X (Supplementary Table 5). [reference (Ref) genome is from un-induced (0 d) Saos2 p21^WAF1/Cip1 cells] **(c)** Novel clonal rearrangements distinguish the "escaped" Saos2 p21^WAF1/Cip1 (ON) from OFF cells [arrows indicate lost (in OFF cells) or rearranged (in "escaped"-ON cells) chromosomes]. The p21^WAF1/Cip1-OFF cells (control), were mainly hypotriploid (51-56 chromosomes) and shared most of the characteristic structural chromosome aberrations of the parental Saos2 cell line.[3] Compared to these cells, the "escaped" ones remained hypo-triploid but displayed at least 10 novel clonal structural or numerical aberrations affecting chromosomes 2, 3, 5, 8, 11, 13, 14, 20, 21 and X. Large portions of chromosomes X and 13 were lost in 90% of the "escaped" cells, confirming the aCGH findings. Furthermore, differential imbalances of chromosomes 5 and X between Saos2 p21^WAF1/Cip1 ON cells and the controls were observed. In "escaped" (ON) cells, an additional inverted duplication of 5p was also present in 90% of the examined nuclei. **(d)** The Saos2 p21^WAF1/Cip1 ON cells exert significantly higher rates (two fold) of random structural CIN/chromosome as compared to controls. (CIN:chromosomal instability) **(e)** Genomic distribution of breakpoints of random structural chromosome anomalies. Telomeric regions were found to be most frequently affected by fusions, translocations and tandem duplications of large chromosome segments. As unidentified ones were categorized the non-telomeric, non centromeric genomic rearrangements in which the cytogenetic bands of their breakpoints remained obscure. **(f)** "Escaped" Saos2 p21^WAF1/Cip1 cells exhibit increased karyotypic

aberrations relative to non-induced cells. Comparative pseudo-colored M-FISH/SKY karyograms of 10 non-induced (OFF) Saos2 p21^WAF1/Cip1 cells (588 chromosomes) and 10 "escaped" (ON) ones (639 chromosomes), for the evaluation of whole genome structural CIN at the 350 chromosome band level. Arrows (and dashed rectangles) indicate representative non-clonal random structural rearrangements (unique anomalies encountered in a single cell). The "escaped" p21^WAF1/Cip1 expressing cells (ON) displayed significantly higher rates of genome wide, random structural chromosomal rearrangements. *ON cells (upper panel):* Cells #1 and #7, from the Saos2 p21^WAF1/Cip1 OFF panel, represent a minor subclone (20%) of this population because they share a distinctive clonal rearrangement affecting a derivative chromosome X and a deletion of 12p. Cells #3 and #5, belong to a second subclone of the control cells that is characterized by a deletion of a rearranged chromosome 19. The remaining non-induced (OFF) p21^WAF1/Cip1 cells #2, #4, #6, #8 and #10, display a homogeneous karyotypic constitution and represent the major clone. Cell #9 is a polyploid product of whole genome endoreduplication of the major clone of Saos2 p21^WAF1/Cip1 OFF cells. *"Escaped"-OFF cells (lower panel):* Cells #1 and #6 differ from the majority of the "escaped" (ON) population as they share a clonal inverted duplication of the long arm of chromosome 21. In addition, cells #2, #4 and #9, have lost a marker translocation der(9) t(5;9) that was replaced by a deletion 9p and acquired clonally an extra translocated der(22)t(20;22). A unique subclonal finding in Cells #3 and #10, of the "escaped" (ON) cells is the persistence of der(9)t(5;9). Cells #5 and #7 represent two different endoreduplicated ON subclones, characterized by unique structural abnormalities of chromosomes 7, 15 and 6 respectively. The karyotypic constitution of cell #8, resembles that of the control population and justifies the presence of an additional subclone that does not exceed the 10% of the "escaped" (ON) cells. (CIN:chromosomal instability)
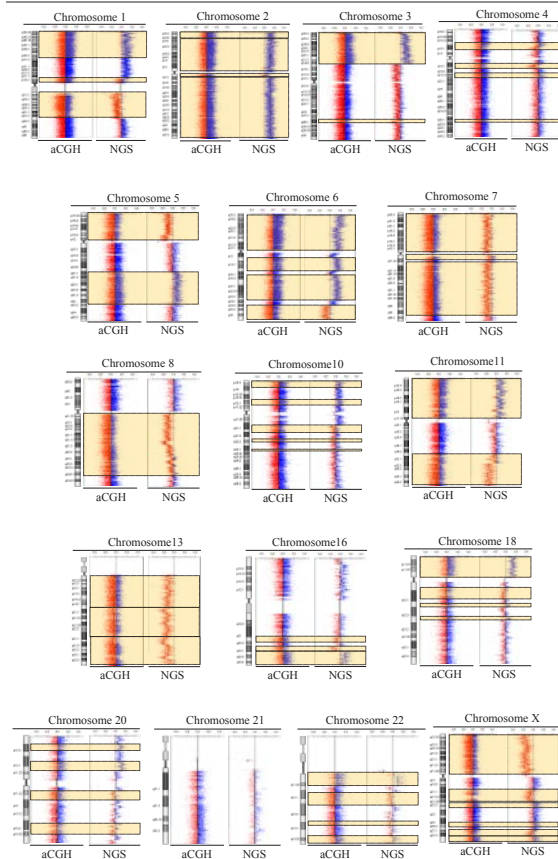
Supplementary Figure 5 Correlation between aCGH replicates and corroboration with the cytogenetically detectable novel clonal alterations in Saos2 p21 cells (* see also Fig. 8f). [reference (Ref) genome is from un-induced (0 d) Saos2 p21$^{WAF1/Cip1}$ cells]
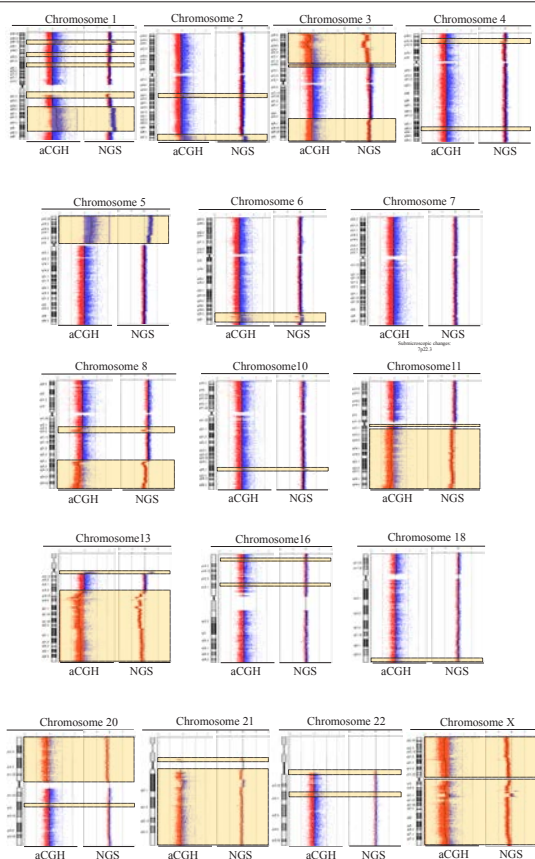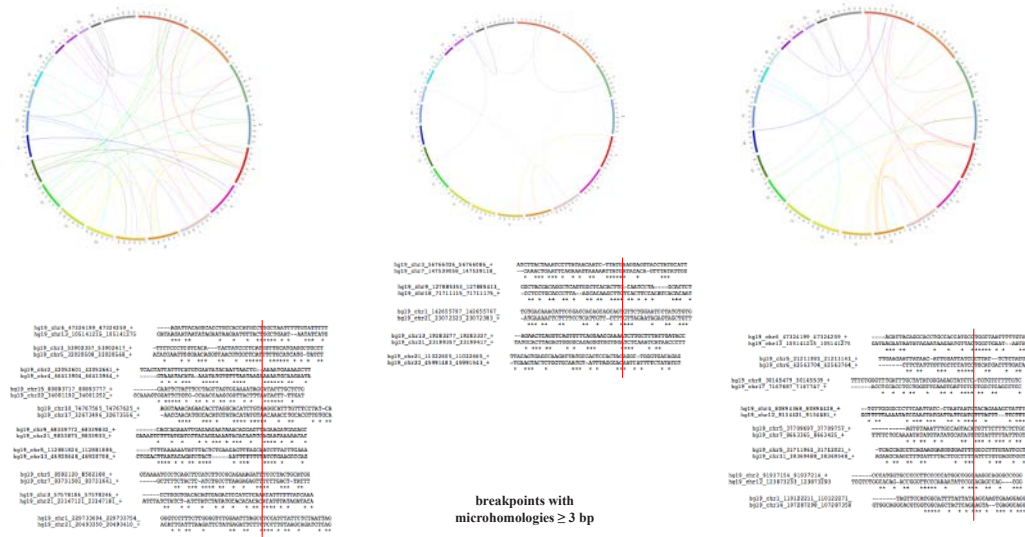
Supplementary Figure 6 Correlation between aCGH and deep sequencing in Saos2 (a) and Li-Fraumeni (b) cells (Next Generation Sequencing: NGS) analyses. Data from all replicates for each application were averaged before comparison.
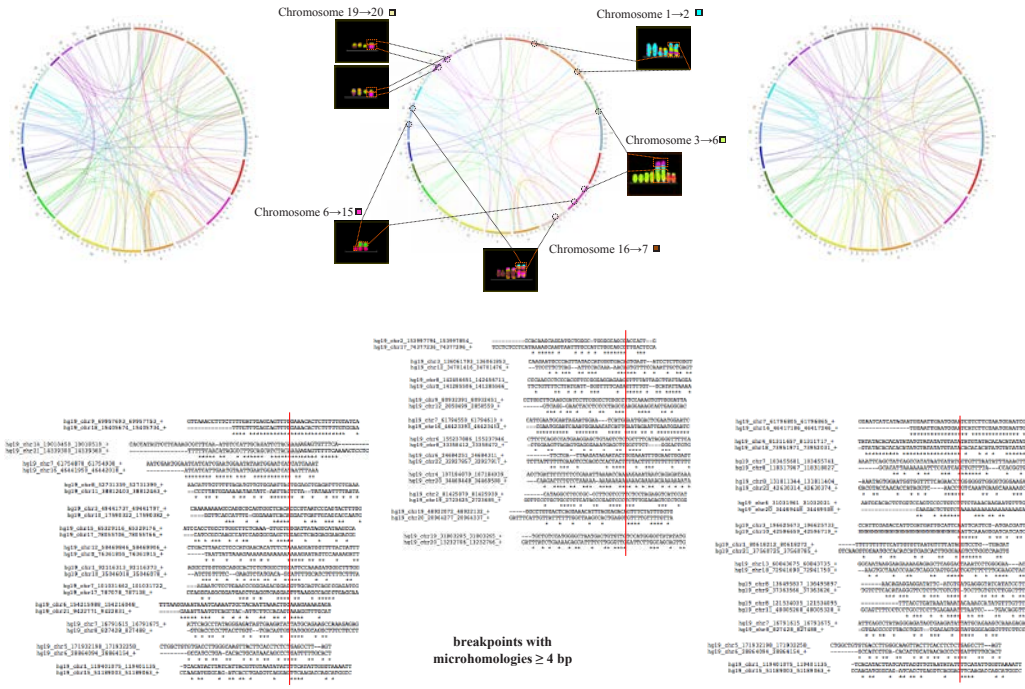
Supplementary Figure 7 Novel chromosomal rearrangements and microhomology regions related to breakpoints in (a) Saos2 and (b) Li-Fraumeni cells. Circos diagrams depicting novel chromosomal rearrangements in "escaped" Saos2 (a) and Li-Fraumeni (b) p21$^{WAF1/Cip1}$ Tet-ON expressing cells, respectively, revealed by deep sequencing (human chromosomes are located at the perimeter). Data from two biological replicates are depicted. Circos in the middle show shared chromosomal rearrangements by the two Saos2 (a) and Li-Fraumeni (b) p21$^{WAF1/Cip1}$ Tet-ON biological replicates. Breakpoints employing micro-homologies ≥ 4bp in Saos2 (a) and ≥ 3bp in Li-Fraumeni (b) p21$^{WAF1/Cip1}$ Tet-ON cells, respectively, are also presented below each circus diagram. Cytogenetic analyses (see also Supplementary Fig S4) confirming NGS data on breakpoints in the "escaped" Saos2 p21$^{WAF1/Cip1}$ Tet-ON expressing cells are also shown. Asterisk (a) denotes breakpoint that does not encompass a micro-homology. Continuous red line denotes position of breakpoints.
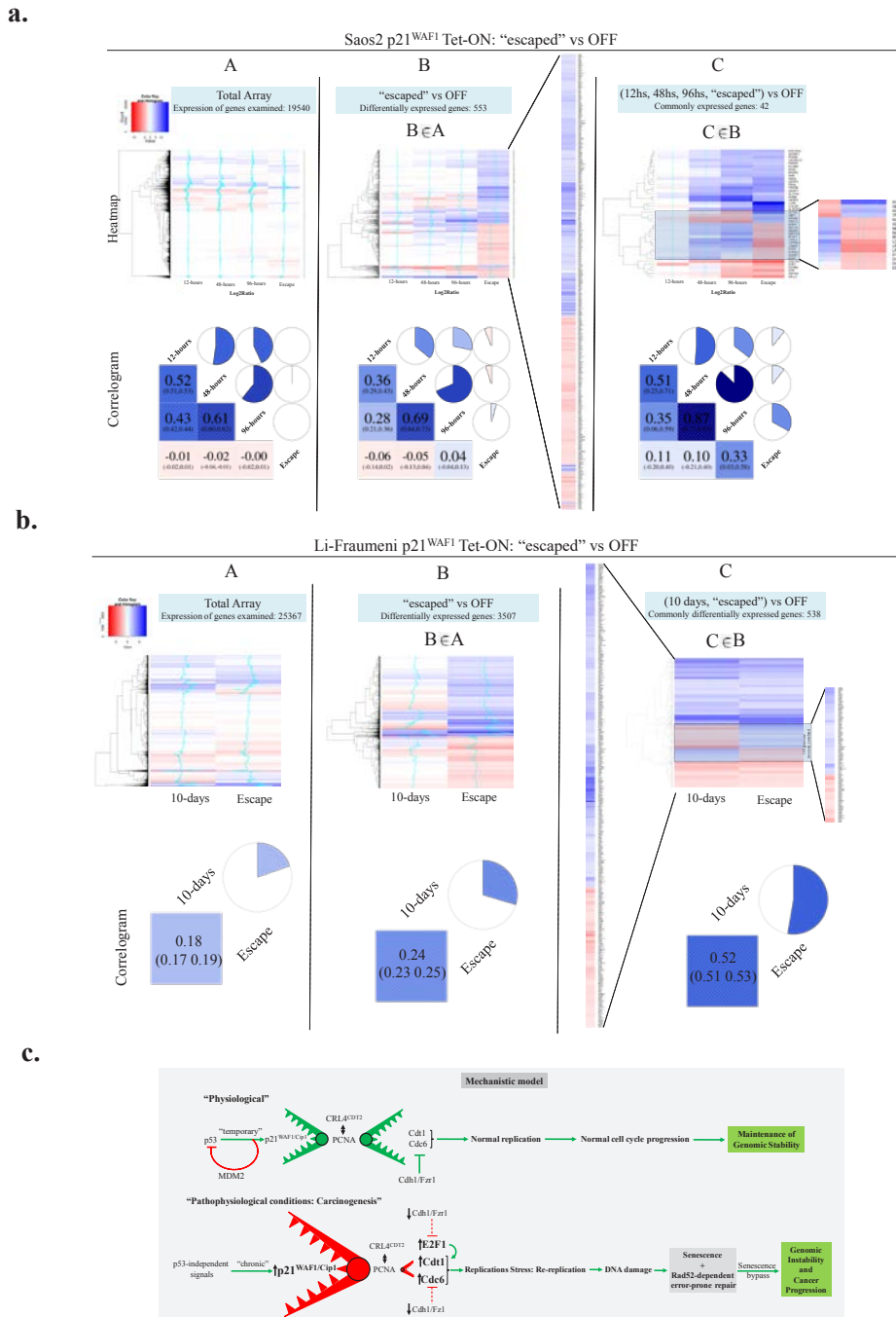
Supplementary Figure 8 Relative gene expression levels (log-2 ratios) at 12, 48, 96-hs after p21$^{WAF1/Cip1}$-induction as well as "escaped" versus OFF cells in (a) Saos2 and relative gene expression levels (log-2 ratios) at 10 days after p21$^{WAF1/Cip1}$-induction as well as "escaped" versus OFF in (b) Li-Fraumeni cells. (c) Proposed model. (a) A: Relative expression of all measured genes (19540) at each depicted time-point as compared to non-induced cells (OFF). The correlogram at the bottom which presents the Pearson correlation coefficient among the 4 datasets illustrates that the overall gene-expression of the "escaped" population is non-correlated (~0 correlation coefficient) to the three prior time points, which amongst them present a high degree of correlation. B: Relative expression of genes presenting differential expression ($p < 0.05$) in the "escaped" cells in relation to OFF (553 genes). The correlogram at the bottom illustrates the absence of correlation between the "escaped" population with the three early time points (12, 48, 96hs). C: Relative expression of commonly differentially expressed genes (42) ($p < 0.05$) at each time-point versus OFF. Special interest present the 16 out of 42 marked genes whose expression levels are reversed at the "escaped" population in comparison to the previous time-points. **(b)** The same heatmaps are presented for Li-Fraumeni cells. A: Relative expression of all measured genes (25367) at each depicted time-point as compared to non-induced cells (OFF). B: Relative expression of genes presenting differential expression ($p < 0.05$) in the "escaped" cells in relation to OFF (3507 genes). C: Relative expression of commonly differentially expressed genes (538) ($p < 0.05$) at each time-point versus OFF. Special interest present the 154 out of 538 marked genes whose expression levels are reversed at the "escaped" population in comparison to 10-days. **(c)** Proposed model depicting prolonged p53-independent p21 oncogenic action (for additional mechanistic explanations see discussion). Under "physiological" conditions, MDM2 degrades p53.[4,10] Dashed lines depict ineffective pathway.

Supplementary Figure 9 Unprocessed blots/gels employed in the current manuscript.

SUPPLEMENTARY INFORMATION

Supplementary References
1. Miyazaki, K. *et al*. A novel HECT-type E3 ubiquitin ligase, NEDL2, stabilizes p73 and enhances its transcriptional activity. *Biochem Biophys Res Commun* **308**, 106-113 (2003).
2. Hanamoto, T. *et al*. Identification of protein kinase A catalytic subunit beta as a novel binding partner of p73 and regulation of p73 function. *J Biol Chem* **280**, 16665-16675 (2005).
3. Sakellariou, D., Chiourea, M., Raftopoulou, C. & Gagos, S. Alternative lengthening of telomeres: recurrent cytogenetic aberrations and chromosome stability under extreme telomere dysfunction. *Neoplasia* **15**, 1301-1313 (2013).

Supplementary Table legends

Supplementary Table 1 Molecules involved in key cellular processes displaing bimodality in cancer.
Supplementary Table 2 Results from mRNA expression analysis on the Illumina whole-genome HumanHT-12 v4.0 arrays, showing gene transcripts affected at 12h, 48h and 96h upon sustained p21$^{WAF1/Cip1}$ induction in Tet-ON, Saos2-p21$^{WAF1/Cip1}$. Three biological replicates (n=3) were used for the analysis of each time point (0,12,48,96).
Supplementary Table 3 Results from mRNA expression analysis on the Illumina whole-genome HumanHT-12 v4.0 arrays, showing gene transcripts (from Table 2) responding early upon sustained p21$^{WAF1/Cip1}$ induction in Tet-ON, Saos2-p21$^{WAF1/Cip1}$. Three biological replicates (n=3) were used for the analysis of each time point (0,12,48,96).
Supplementary Table 4 Results from mRNA expression analysis on the Illumina whole-genome HumanHT-12 v4.0 arrays, showing gene transcripts (from Table 2) responding at intermediate time upon sustained p21$^{WAF1/Cip1}$ induction in Tet-ON, Saos2-p21$^{WAF1/Cip1}$. Three biological replicates (n=3) were used for the analysis of each time point (0,12,48,96).
Supplementary Table 5 Results from mRNA expression analysis on the Illumina whole-genome HumanHT-12 v4.0 arrays, showing gene transcripts (from Table 2) responding late upon sustained p21$^{WAF1/Cip1}$ induction in Tet-ON, Saos2-p21$^{WAF1/Cip1}$. Three biological replicates (n=3) were used for the analysis of each time point (0,12,48,96).
Supplementary Table 6 Results from proteomic analysis showing proteins affected at 12h, 48h and 96h upon sustained p21WAF1/Cip1 expression in Tet-ON, Saos2 p21$^{WAF1/Cip1}$. Data show the mean of two biological replicates for each time point (0,12,48,96).
Supplementary Table 7 Results from proteomic analysis showing proteins (from Supplementary Table 6) responding early upon sustained p21WAF1/Cip1 expression in Tet-ON, Saos2 p21$^{WAF1/Cip1}$. Data show the mean of two biological replicates for each time point (0,12,48,96).
Supplementary Table 8 Results from proteomic analysis showing proteins (from Supplementary Table 6) responding at intermediate time point upon sustained p21$^{WAF1/Cip1}$ expression in Tet-ON, Saos2 p21$^{WAF1/Cip1}$. Data show the mean of two biological replicates for each time point (0,12,48,96).
Supplementary Table 9 Results from proteomic analysis showing proteins (from Supplementary Table 6) responding late upon sustained p21$^{WAF1/Cip1}$ expression in Tet-ON, Saos2 p21$^{WAF1/Cip1}$. Data show the mean of two biological replicates for each time point (0,12,48,96).
Supplementary Table 10 Results from aCGH analysis in Li-Fraumeni p21$^{WAF1/Cip1}$ Tet-ON "escape" vs non-induced (OFF) cells (Agilent G3 CGH 1M arrays). "Escaped" cells acquired chromosomal aberrations, in the form of gains and losses that ranged in size from approximately 1.75Kb to 92Mb.
Supplementary Table 11 Results from aCGH analysis in Li-Fraumeni p21$^{WAF1/Cip1}$ Tet-ON "escape" vs non-induced (OFF) cells (Agilent G3 CGH 1M arrays). "Escaped" cells acquired chromosomal aberrations, in the form of gains and losses that ranged in size from approximately 1.26Kb to 48Mb.
Supplementary Table 12 Results from cytogenetic analysis in "escaped" (ON) Saos2 p21$^{WAF1/Cip1}$ cells depict the predominance of breakpoints of random re-arrangements in Fragile Sites (FSs).
Supplementary Table 13 Chromosomal coordinates of breakpoints found by deep sequencing in Saos2 p21$^{WAF1/Cip1}$ Tet-ON.
Supplementary Table 14 Chromosomal coordinates of breakpoints found by deep sequencing in Li-Fraumeni p21$^{WAF1/Cip1}$ Tet-ON.
Supplementary Table 15 Shared breakpoints found in the Saos2 p21$^{WAF1/Cip1}$ Tet-ON (from Table 13) and Li-Fraumeni p21$^{WAF1/Cip1}$ Tet-ON (from Table 14), respectively.
Supplementary Table 16 Breakpoints with microhomologies (MHs) in Saos2 p21$^{WAF1/Cip1}$ Tet-ON (69% of total breakpoints) and Li-Fraumeni p21$^{WAF1/Cip1}$ Tet-On (~71-80% of total breakpoints) escaped cells. (red line denotes position of breakpoint)
Supplementary Table 17 Molecules displaying up-regulation in Saos2 p21$^{WAF1/Cip1}$ Tet-ON escaped cells, stemness abilities and proposed to promote carcinogenesis.
Supplementary Table 18 Molecules displaying up-regulation in Saos2 p21$^{WAF1/Cip1}$ Tet-ON escaped cells and proposed to promote carcinogenesis.
Supplementary Table 19 Molecules found expressed in Saos2 p21$^{WAF1/Cip1}$ Tet-ON escaped cells and proposed to display a bimodality in cancer promotion.
Supplementary Table 20 Molecules displaying up-regulation in Li-Fraumeni p21$^{WAF1/Cip1}$ Tet-ON escaped cells, stemness abilities and proposed to promote carcinogenesis.
Supplementary Table 21 Molecules displaying down-regulation in Li-Fraumeni p21$^{WAF1/Cip1}$ Tet-ON escaped cells.
Supplementary Table 22 Molecules found expressed in Li-Fraumeni p21$^{WAF1/Cip1}$ Tet-ON escaped cells and proposed to display a bimodality in cancer promotion.
Supplementary Table 23 List of antibodies employed in immunohistochemistry, immunofluorescence, immunoblotting, immunoprecipitation and chromatin.
Supplementary Table 24 Primers and annealing temperatures used in real time (RT)-PCR and ChIP analyses.
Supplementary Table 25 Statistics Source Data.

Supplementary Video legends

Supplementary Video 1 Dividing Saos2 p21$^{WAF1/Cip1}$ Tet-OFF cells.
Supplementary Video 2 Senescent Saos2 p21$^{WAF1/Cip1}$ Tet-ON cells.
Supplementary Video 3 Senescent and dying Saos2 p21$^{WAF1/Cip1}$ Tet-ON cells.
Supplementary Video 4 Re-replicating Saos2 p21$^{WAF1/Cip1}$ Tet-ON cells.
Supplementary Video 5 Escaped and diving Saos2 p21$^{WAF1/Cip1}$ Tet-ON cells.